SEARCH FOR SUPERSYMMETRY USING WEAK BOSON FUSION PROCESSES IN PROTON-PROTON COLLISIONS AT THE LARGE HADRON COLLIDER

A Dissertation

by

WILL HOGAN FLANAGAN

Submitted to the Office of Graduate and Professional Studies of
Texas A&M University
in partial fulfillment of the requirements for the degree of

DOCTOR OF PHILOSOPHY

Chair of Committee,	Teruki Kamon
Committee Members,	Bhaskar Dutta
	Dave Toback
	Sherry Yennello
	Othmane Bouhali
Head of Department,	George Welch

August 2014

Major Subject: Physics

ABSTRACT

In 2012, the Large Hadron Collider at CERN (LHC) collided protons at an unprecedented center-of-mass energy of 8 TeV. With data corresponding to a total integrated luminosity of 19.7 fb^{-1}, the Compact Muon Solenoid (CMS) collaboration is studying various Standard Model processes as well as searching for Beyond the Standard Model processes through a plethora of distinct projects. This dissertation searches for Supersymmetry using weak boson fusion processes. These processes provide a unique opportunity to access the electroweak sector of supersymmetry. Though well motivated, this search finds no excess above the Standard Model. Exclusion limits are obtained in the context of electroweakino masses at the 95% confidence level.

DEDICATION

To my parents for giving me my opportunities. To my brothers for toughening me up. To my friends for being the best group of friends that a guy could ask for. To Danielle for everything. To Kamon-sama for inspiring me to become a particle physicist.

If I have seen further it is by standing on ye shoulders of Giants

–Isaac Newton

ACKNOWLEDGEMENTS

I would like to thank all those who have helped to get to this point.

Mary Wakamoto, for helping to guide and mold my interests.

Keith MacGregor for being a wonderful first research advisor.

Roberto Cassini, Emily CoBabe-Ammann, Mark Rast, Nicole vad der Bliek, Jayadev Rajagopal, Ryan Campbell, and John Bally for guiding my early interest in Astronomy.

Teruki Kamon for inspiring me to pursue particle physics.

Sherry Yennello for making the encounter possible.

Bhaskar Dutta for many great conversations.

Uriel Nauenberg for showing me a career to emulate.

Alfredo Gurrola, Jim Pivarski, Bernadette Heyburn, Taylan Yetkin, and Hongxuan Liu for really showing me the ropes early on.

Alfredo Gurrola for continuing to show me the ropes.

Ali Celik, Andrés Delannoy, Nitish Dhingra, Andrés Flórez, Tathagata Ghosh, Jason Gilmore, Kenichi Hatakeyama, Heshani Jayatissa, Amandeep Kalsi, Jieun Kim, Shuichi Kunori, Eduardo Luiggi, Daniele Marconi, Angela Marotta, Sho Maruyama, Andrew Melo, Roy Montalvo, Alexx Perloff, Denis Rathjens, Jeff Roe, Alexei Safonov, Austin Schneider, Kuver Sinha, Sinjini Sengupta, Indara Suarez, Aysen Tatarinov, Lukas Vanelderen, Kechen Wang, Sean Wu, Shilei Zang (and anyone I rudely left out) for being a pleasure to work with.

Nick Diaczenko for great coffee and mediocre jokes.

Dave Toback for great career advise.

Karol Lang and Jack Ritchie for inviting me to start the next great chapter.

TABLE OF CONTENTS

Page

LIST OF FIGURES

FIGURE Page

LIST OF TABLES

1. INTRODUCTION: THE STANDARD MODEL AND BEYOND

This dissertation is organized as follows: This section will highlight the status quo of particle physics and our motivation for carrying out this search. Section 2 will highlight the experimental apparatus used. Section 3 will present the dataset. Section 4 will discuss our physics objects used in the analysis. Section 5 will give the detailed analysis, results, and new limits to simplified SUSY models. Section 6 will conclude.

1.1 The Standard Model of Particle Physics

The Standard Model of Particle Physics (SM) is one of mankind's most impressive accomplishments. It describes the unification of the electromagnetic and weak interations. To acheive this, it combined the work of Glashow, Weinberg, and Salam [1][2][3] and many others to provide a concise framework for all known fermions and bosons, which are the building blocks of all matter as well as the force carriers, respectively. The photon, the force carrier of the electromagnetic force, is governed by a global symmetry described by the U(1) group. The $W^{\pm}$ and Z^0 bosons and gluons are similarly governed by a global symmetry of the SU(2) and SU(3) groups, respectively. Glashow, Weinberg, and Salam in their formulation of the Standard Model postulated the existence of a set of symmetries governed by the direct product of these three groups:

$$U(1) \times SU(2)_L \times SU(3) \tag{1.1}$$

The L denotes that SU(2) symmetry applies only to left handed fermions. The Lagrangian which obeys this symmetry at every local point governs the masses and

interactions of our theory from nuclear physics to cosmology. From the Lagrangian we can derive particle trajectories, interaction probabilities, and all other measurable properties of our system.

The Standard Model has had many confirmed predictions, including the existence of gluons [4][5], the existence of and later precise masses of $W^{\pm}$ and Z^0 bosons [6], the top quark [7][8], and the tau neutrino [9]. Most recently, it appears that we have discovered a scalar boson which closely resembles the much anticipated Higgs boson, which was the last prediction of our Standard Model Lagrangian [10][11]. Finding this boson roughly where it was expected to be is yet another testament to the predictive power of our theory. This discovery is nonetheless exciting as it appears to be the first discovered scalar boson. If this boson has the other characteristics of the Standard Model prediction, this is widely regarded as the final great accomplishment of this successful theory. This discovery also paves the way for many precise measurements which will either solidify our understanding of the Standard Model or raise fascinating questions for future experiments.

1.2 Motivations for Physics Beyond the Standard Model

Though extraordinarily successful, the Standard Model of Particle Physics cannot be a complete theory for a number of reasons.

Theoretically, the top mass diverges quadratically unless cancelled by a supersymmetric extension to the Standard Model [12]. Furthermore, the Standard Model has no explanation for other pressing questions such as neutrino mass hierarchy and matter anti-matter asymmetry.

Experimentally, there are many measurements for which the SM prediction is not in agreement with precise measurements. One such example is the anomalous magnetic moment of the muon. This quantity is known both theoretically and exper-

imentally to better than one in a million precision. The disagreement between the SM prediction and the experimental value is roughly 2.2-2.7 standard deviations according to measurements at the Brookhaven Alternating Gradient Synchrotron [13]. It has been widely noted that loop corrections from supersymmetric particles pose one possible solution to this discrepancy (see Figure 1.1). It is worth noting that any proposed extension to the SM has the challenge of solving such discrepancies without adding significant loop corrections to measurements which are already in nice agreement with the SM (see Figure 1.2 and [14][15] for one such example with the $b \to s\gamma$ cross section). As various experiments make more and more precise measurements, the number of challenges to the SM increase. It was recently noted that there is an 3.4 standard deviation excess of $\bar{B} \to D^{(*)}\tau^-\nu_\tau$ decays within the BaBar experiment [16].

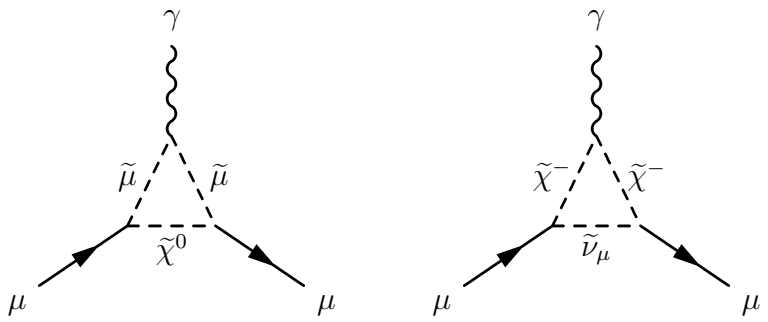

Figure 1.1: One loop SUSY corrections to the muon $(g-2)_\mu$ given by gauginos and sleptons which have the possibility of correcting the anomalous magnetic moment of the muon.

The most egregious fault within the SM is the theory's inability to explain the existence of a cold dark matter (CDM) particle. CDM is a weakly interacting heavy particle which has been observed by astronomers indirectly through discrepancies in stellar rotation curves and gravitational lensing, among various other methods.

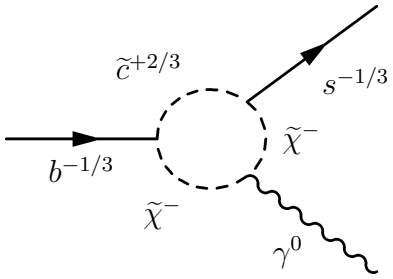

Figure 1.2: A one loop SUSY corrections to the $b \to s\gamma$ given by charginos and a charm squark. The Belle and BaBar experiments have already found this rate to be in excellent agreement with the Standard Model[14][15] without assuming any physics beyond the Standard Model.

The relic density of CDM has been measured to a high degree of precision by the WMAP, and later Planck, experiments using the angular spectrum of the cosmic microwave background [17][18]. The ability to predict a dark, heavy, and stable particle with minimal assumptions is one of the key motivations for R-parity conserving supersymmetry (SUSY) as will be discussed in the next section.

1.3 Supersymmetry

Supersymmetry predicts the existence of a SUSY partner to each SM particle with similar characteristics except a difference in spin by 1/2 and a differing mass, effectively doubling the list of fundamental particles. In addition to canceling the quadratic divergence of the Higgs mass, SUSY has the ability to unify the gauge couplings at GUT scale ([19] and Figure 1.3 from [20]). This implies that besides combining electromagnetic and strong interactions into one cohesive theory, these forces may be low energy manifestations of a more fundamental force at higher energy scales. Furthermore, the lightest SUSY particle (LSP) is stable when R-parity is conserved as a $\mathbb{Z}_2$ symmetry. R-parity is defined as:

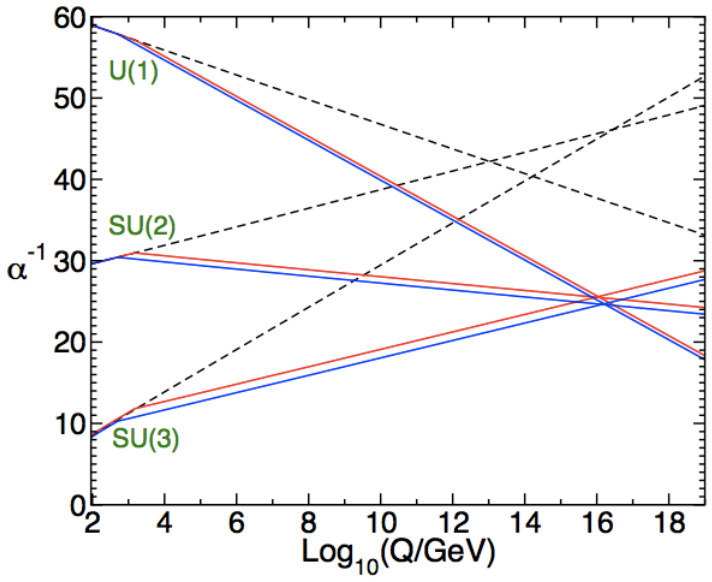

Figure 1.3: Inverse Standard Model gauge couplings approaching GUT scale with and without loop corrections from MSSM. Taken from p. 61 of [20].

$$R = (-1)^{2j+3B+L} \tag{1.2}$$

where j, B, and L are the spin, baryon, and lepton quantum numbers. Since $2j + 3B + L$ is an even number for all Standard Model particles, all SM particles have an R-parity of +1. As SUSY particles vary from their SM partner by $j \pm \frac{1}{2}$ while maintaining the same baryon and lepton numbers, $2j + 3B + L$ becomes odd and therefore R-parity is -1 for all SUSY particles. As $-1 \neq 1 \times 1$, SUSY particles may not decay strictly into SM particles; that is each SUSY particle must always decay into at least one more SUSY particle. For this reason, our LSP is stable[1]. When the LSP is also weakly interacting and heavy, it becomes a plausible CDM candidate as previously noted.

[1]It is also worth noting that the assumption of R-parity conservation places no constraint on the Standard Model since $1 = 1 \times 1$.

The neutralinos, denoted as $\tilde{\chi}_n^0$, are a mixture of Bino ($\tilde{B}$), Wino ($\tilde{W}$), and Higgsino ($\tilde{H}$) (see Appendix B). In the search presented here, benchmark points with the lightest neutralino ($\tilde{\chi}_1^0$) as the LSP will be used. The underlying composition of our $\tilde{\chi}_n^0$ plays a vital role in whether our LSP provides the observed dark matter relic density [21]. For example, a $\tilde{\chi}_n^0$ that is purely $\tilde{B}$ has too small of a self annihilation cross section and as a result provides a dark matter relic density that is too large. Alternatively, pure $\tilde{W}$ and $\tilde{H}$ would annihilate strongly enough to give a dark matter relic density that is much smaller than observed (assuming standard cosmological models).

1.4 The Status Quo of New Physics Searches

A plethora of searches for SUSY particles have been conducted by both the CMS and ATLAS experiments with roughly 5fb^{-1} of 7 TeV data in 2011 and 20fb^{-1} of 8 TeV data in 2012. These searches have ruled out large portions of minimal SUSY phase space (mSUGRA, mGMSB, mAMSB) [22][23][24]. Many regions that were previously well motivated by various measurements such as the anomalous magnetic moment and dark matter relic density are now all but ruled out in SUSY parameter space with minimal assumptions [25]. In particular, the stau neutralino co-annihilation region is all but excluded in mSUGRA [26]. The 95% confidence level exclusions are particularly restrictive in the context of SUSY parameter space where squarks and gluinos are produced directly with subsequent cascade decays containing high energy jets as can be seen in Figure 1.4. One possibility that remains is that colored SUSY particles may be too heavy to be produced directly at current LHC energies. This means that only lighter, electroweakly interacting SUSY particles are within reach of the LHC. As a result, SUSY may have alluded detection by having a smaller cross section than expected (by not having color charge) and being insensitive

to common "jet+$\not\!\!E_{\mathrm{T}}$" SUSY searches. As we will see in the next section, the search presented here is well-suited to exactly such a scenario and will aim to detect these electroweakling interacting SUSY particles (EWKinos) directly without relying on cascade decays from heavier colored particles. Furthermore, WBF processes can also serve as an excellent probe for compressed scenarios, which may allude other standard SUSY searches [27].

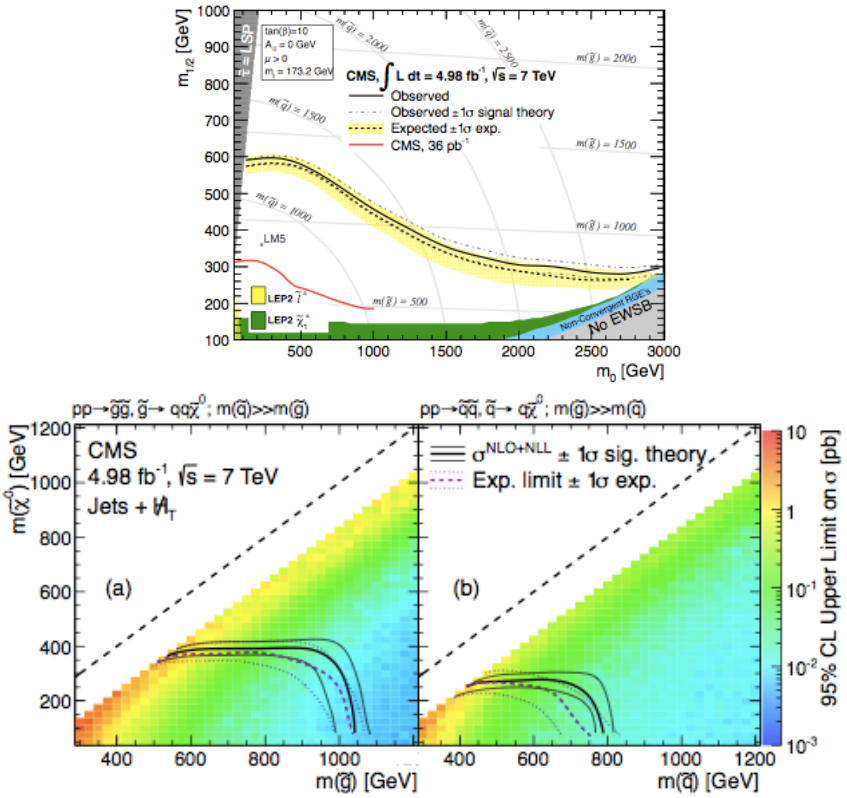

Figure 1.4: 95% confidence level exclusions to SUSY parameter space in the context of mSUGRA (above) and simplified model scans for gluinos and squarks (below).

2. THE CMS DETECTOR AT THE CERN LHC

This section will present our experimental apparatuses, chiefly the CERN Large Hadron Collider and the Compact Muon Solenoid Detector.

2.1 CERN

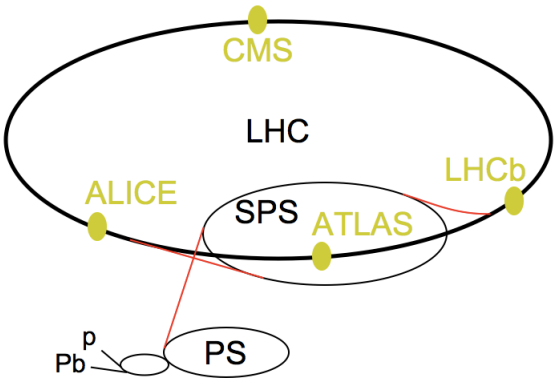

Figure 2.1: Physical layout of the LHC experiment. The beam transfer lines are shown in red while the four LHC collision points are shown in yellow.

Particle physicists are excellent recyclers. The Large Hadron Collider (LHC) is build out of many past groundbreaking experiments. The 17 mile tunnel which comprises the main ring of the LHC was originally constructed for the Large Electron-Positron (LEP) Collider, which made precise measurements of the $W^{\pm}$ and Z^0 bosons throughout the 1990s. This main ring is fed by the Super Proton Synchrotron (SPS), which first discovered the $W^{\pm}$ and Z^0 bosons in the early 1980s. SPS is, in turn, fed by the Proton Synchotron, which has fed many great experiments since the 1950s

[1]It is worth noting that particle physicists are also great sharers. Components of the LHC and its detectors are made in many countries and continents, converging to produce an unparalleled machine.

including the Intersecting Storage Rings, which was the world's first hadron collider[1]. The Proton Synchrotron accelerates protons to 28 GeV. The SPS accelerates those same protons to 450 GeV. Finally the LHC accelerates those proton beams to 4 TeV, leading to a center-of-mass energy, $\sqrt{s}$, of 8 TeV (Figure 2.1).

2.2 The Large Hadron Collider

The LHC collides protons at four points along the main ring (Point 1, Point 2, Point 5, and Point 8) [28]. There are seven detectors placed at these interaction points. At Point 1, we have the A Toroidal LHC Apparatus (ATLAS) and Large Hadron Collider forward (LHCf) experiments. ATLAS is a general use detector whereas LHCf is studying ultra-high-energy cosmic rays. At Point 2 we have A Large Ion Collider Experiment (ALICE), specialized for lead-proton and lead-lead collisions. At Point 5 we have the Compact Muon Solenoid (CMS) and the TOTal Elastic and diffractive cross section Measurement (TOTEM). CMS is a general use detector and the focus of all following sections. TOTEM is an experiment for accurate measurements of luminosity and diffraction. At Point 8 we have the LHCbeauty (LHCb) experiment which is specialized for b-physics measurements and the Monopole and Exotics Detector (MoEDAL) searching for magnetic monopoles and stable, ionizing massive particles.

The LHC collided protons at a center-of-mass energy, $\sqrt{s}$, of 7 TeV in 2010 and 2011 then 8 TeV in 2012. The integrated luminosity reached 36 pb^{-1} in 2010, 5 fb^{-1} in 2011, and 23 fb^{-1} in 2012 (see Figure 2.2). As the instantaneous luminosity increased, so did the average number of simultaneous interactions (pileup) as can be seen in Table 2.1. In 2012, there were 21 simultaneous collisions on average. Future LHC runs will reach an instantaneous luminosity that will dwarf that of 2012. In upcoming High Luminosity LHC (HL-LHC) runs (see Figure 2.3) there will

be $\mathcal{O}(140)$ simultaneous collisions, providing a great integrated luminosity but also a great experimental challenges. However, this analysis will focus on the 8 TeV data collected in 2012.

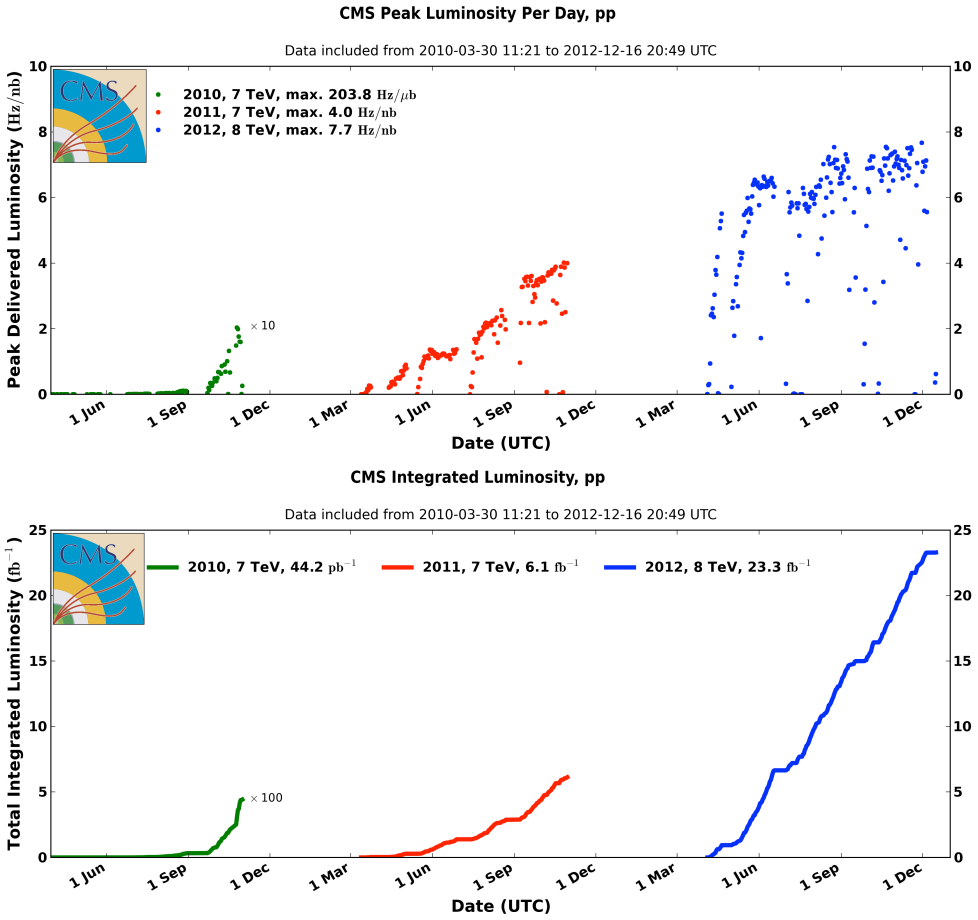

Figure 2.2: The instantaneous (top) and integrated (bottom) luminosities of the past three years of LHC data taking. Note that $\frac{\text{Hz}}{\text{nb}} = 10^{33}\text{cm}^{-2}\text{s}^{-1}$.

Year	$\sqrt{s}$ [TeV]	$\mathcal{L}_{max}$ [cm^{-2} s^{-1}]	$\mathcal{L}_{int}$ [fb^{-1}]	$\mathcal{L}_{int}^{CMS}$ [fb^{-1}]	$<$ PU $>$
2010	7	2.1×10^{32}	0.0442	0.0408	2
2011	7	3.5×10^{33}	6.1	5.6	9
2012	8	7.7×10^{33}	23.3	21.8	21

Table 2.1: The center-of-mass energy, maximum instantaneous luminosity, total integrated luminosity, total recorded luminosity by CMS, and the average number of interactions per bunch crossing for the last three years of LHC operation.

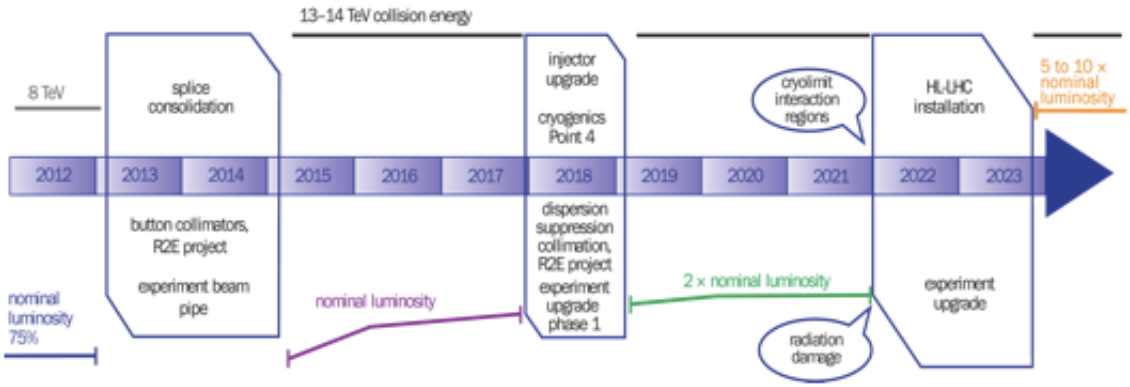

Figure 2.3: Schematic showing the evolution of the LHC experiment. Following the (current) first long shutdown, there will be a nominal luminosity run at $\sqrt{s}$ of 13-14 TeV. Following the second long shutdown, there will be another run of higher luminosity. Following a third long shutdown, the LHC will be ready for High Luminosity (HL) runs, denoted HL-LHC.

2.3 The Compact Muon Solenoid

Of the four detectors along the LHC main ring, two are general use detectors: ATLAS and CMS [Fig 2.4]. Though quite similar in most regards, there are some slight diffierences [29]. The two experiments have notably different magnet systems. ATLAS employs a small (2 Tesla) solenoid magnet just outside the tracking system (but inside the calorimeters) with a toroidal magnet at each endcap (before the muon chambers) [30]. The solenoid magnets bend charged particles moving transverse to the beamline in the azimuthal direction for precise momentum measurements while the toroid magnets bend muons heading to the forward muon detectors. CMS, on the other hand, uses one solenoid magnet which is located outside the calorimeters, leading to interesting constraints on possible detector materials [Sec. 2.3.4]. There are other differences, such as CMS having purely silicon tracking systems while ATLAS employs some non-silicon tracking systems, but both detectors use the same basic strategies.

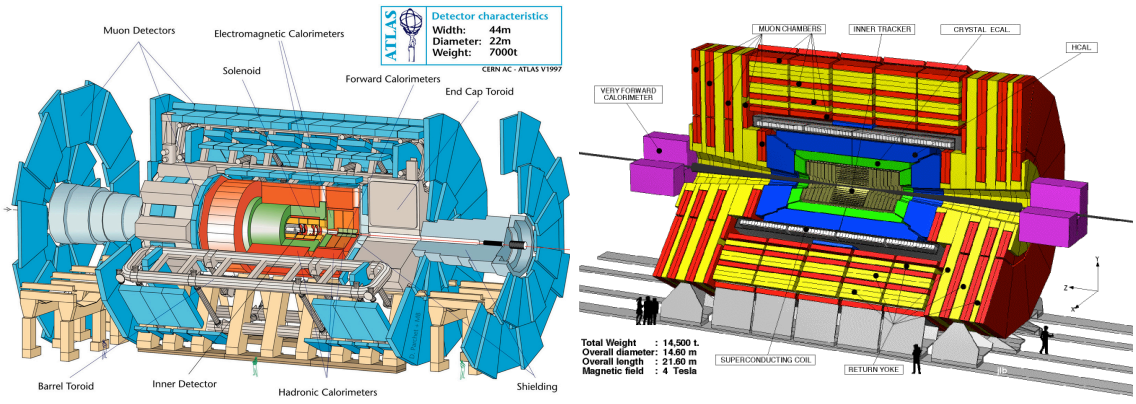

Figure 2.4: Schematics of the ATLAS (left) and CMS (right) detectors. [30, 31]

CMS was designed with four basic requirements [31]:

- Excellent muon identification, including precise momentum, dimuon invariant mass, and charge determination within $|\eta| < 2.5$.
- Excellent track reconstruction of all charged particles, particularly the decay products of b-jets and τ leptons.
- Excellent photon and electron identification, including diphoton/dielectron invariant mass and primary vertex reconstruction and π^0 rejection within $|\eta| < 2.5$.
- Excellent $\not\!\!E_T$ and dijet mass reconstruction within $|\eta| < 5$.

The following sections will reveal how CMS achieves each of these goals by combining various components and subdetectors into one state-of-the-art machine.

2.3.1 The Magnet

One of the most distinguishing features of CMS is the powerful superconducting solenoid magnet (which claims $\frac{1}{3}$ of the experiment's acronym). With an inner radius of 5.9m and and a length of 12.9m, it encompasses much of the detector. Since CMS has no forward toroidal magnet, the solenoid length-to-width ratio is chosen such that the field will give the maximum possible bend to forward muons[1]. Though designed to have a 4 Tesla field, it has been operating at 3.8 Tesla to maximize magnet longevity [32]. Having such a large magnetic field allows for better momentum reconstruction through the curvature of charged particles.

2.3.2 The Tracker

The inner tracker is the first layer of the CMS detector. Rather than capturing particles, it functions by tracing the path of charged particles as they make their

[1]A magnetic field purely in-line with the proton beam would give virtually no '$v \times B$' kick to a forward muon.

way to the calorimeters. By assuming a mass (for an electron, pion, muon, etc), the tracker can accurately reconstruct the momentum of charged particles as they bend within the 3.8T magnetic field. The tracking system is also capable of measuring secondary vertices from long-lived particles such as b-hadrons. Silicon was chosen as the tracking material in order to achieve a balance of granularity, radiation hardness, and speed. Designed to deal with 1000 particles hitting the tracker in every LHC bunch crossing, the CMS tracker is the largest silicon tracker ever built. The inner system is composed of 100x150 μm^2 pixels. The outer system is composed of silicon strips 10 cm x 80 μm (TIB, TID) to 25 cm x 180 μm (TOB, TEC) in size giving coverage to a pseudorapidity of 2.5 (see Fig. 2.5). Though not part of the level 1 or 2 triggering used in this analysis, tracking information is vital to high level muon triggering as will be discussed in section 3 [33]. The tracker is also essential to distinguishing between charged and neutral particles which leave similar energy deposits in the calorimeters such as electrons and photons or charged hadrons and neutral hadrons.

2.3.3 The Electromagnetic Calorimeter

The electromagnetic calorimeter (ECAL) is constructed from lead tungstate ($pbWO_4$) crystals due to lead tungstate's short radiation length, small Moliere radius and radiation hardness (Figure 2.6). The barrel region (EB) extends to $|\eta| < 1.479$ while the endcap region (EE) extends to $|\eta| < 3.0$. The endcap (barrel) crystals begin 1.29m (3.15m) from the nominal interaction point and are 230mm (220mm) long corresponding to 25.8 (24.7) radiation lengths. Most of the endcap region is covered by a preshower detector ($1.653 < |\eta| < 2.6$). The subdetector helps to distinguish electrons from minimum ionizing particles as well as to improve position resolution. Composed of two layers of lead and silicon strip sensors. The lead

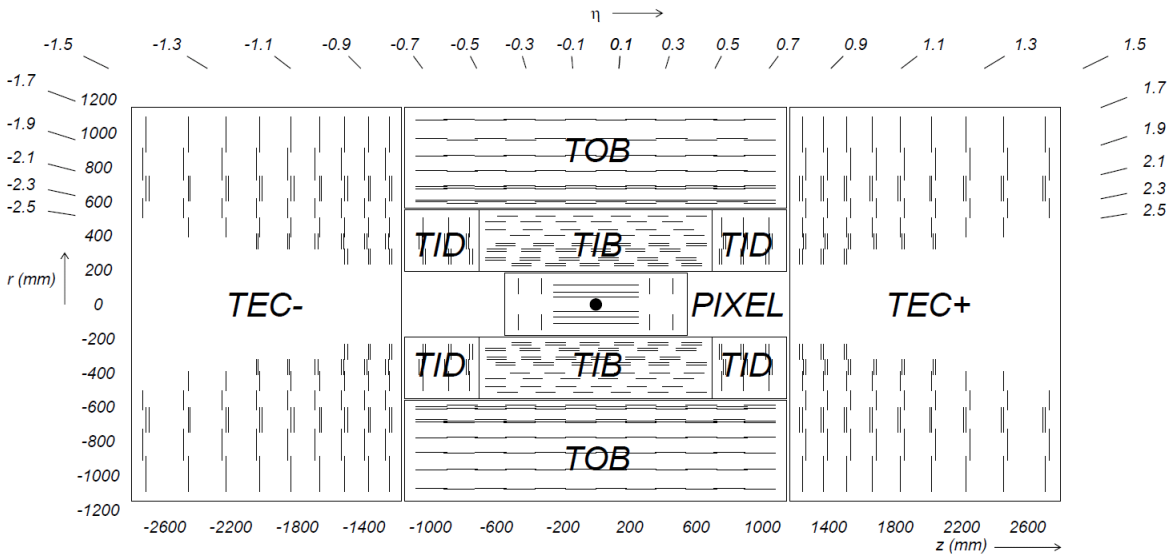

Figure 2.5: Schematic of the tracking system. The innermost region is silicon pixels. The silicon strip tracker is divided between the inner barrel (TIB), inner disk (TID), outer barrel (TOB), and the endcap (TEC) regions. [31]

initiates electromagnetic showers while the silicon sensors measure the resulting energy. Altogether, the ECAL has an energy resolution of 0.5% for 120 GeV electrons. This excellent electron energy resolution helps to reliably reconstruct the underlying electron kinematics and to minimize the systematic uncertainties in our study.

2.3.4 The Hadron Calorimeter

The hadron calorimeter (HCAL) is composed of four distinct regions. The barrel region (HB) covers the pseudorapidity range of $|\eta| < 1.3$ while the endcap region (HE) extends the coverage to a pseudorapidity of 3. A forward calorimeter (HF) further extends the reach to a pseudorapidity of 5 while an outer calorimeter (HO) provides an extra layer of scintillators outside the barrel (Fig. 2.7). HCAL is composed of brass absorber and plastic scintillator tiles. Since our HCAL is within a 4 Tesla magnetic field, brass was chosen due to its non-magnetic nature. HB is installed

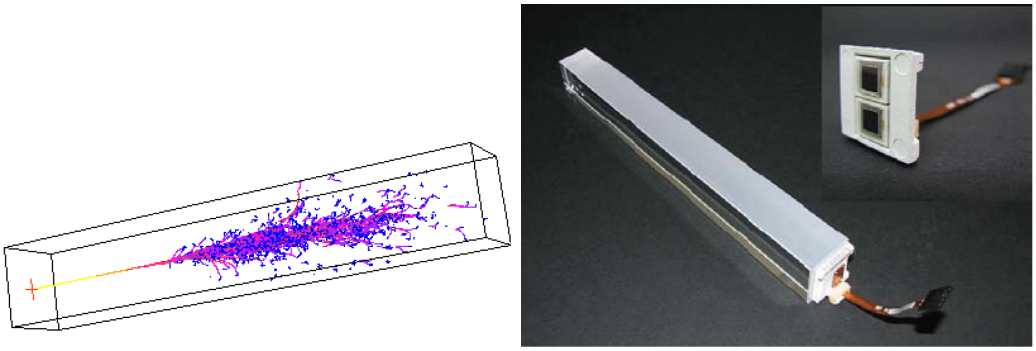

Figure 2.6: A simulated electromagnetic shower created due to the interaction of an electron with an ECAL crystal (left) and a barrel crystal before being assembled into supermodules. [31]

as 36 10° wedges. Since the length is constrained by the outer edge of EB (1.77m) and the inner edge of the magnet coil (2.95m), HO sits just after the magnet coil to capture any additional energy. The HB scintillators are segmented to give a granularity of $\Delta\eta \times \Delta\phi = 0.087 \times 0.087$. HB continues this segmentation to a pseudorapidity of 1.6 where the segmentation becomes a more coarse granularity of $\Delta\eta \times \Delta\phi = 0.17 \times 0.17$ in HE. EB and HB absorbers provide 5.82 interaction lengths at $\eta = 0$ and 10.6 interaction lengths at $|\eta| = 1.3$. EE and HE, less constrained by the magnet and muon system maintain 10 interaction lengths throughout. HF makes use of quartz fibers due radiation hardness and the ability to deal with extremely high rates. HF functions by capturing the Cherenkov light while transiting the quartz fibers. Together, these four HCAL subsystems allow for a hermetic coverage where jets can be reconstructed to a pseudorapidity of ± 5 (see Figure 2.7). This coverage is particularly important to a VBF-type study such as this with two forward jets.

HF also plays a crucial role in measuring luminosity. It does so through a process called 'zero counting'. Since the number of collisions in each bunch crossing is given

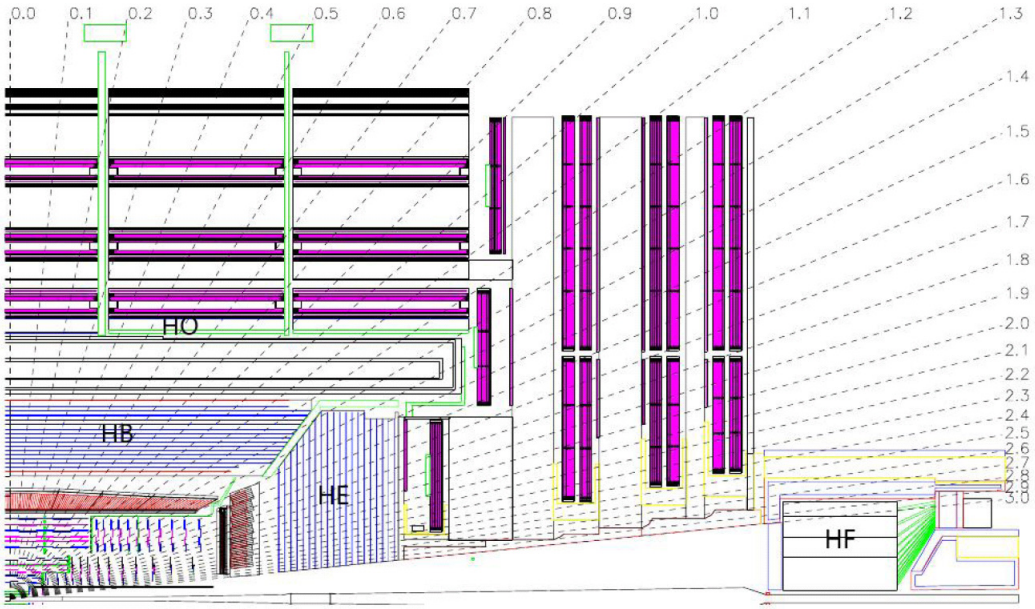

Figure 2.7: Schematic of one quadrant of the CMS detector, showing the positions of the hadron barrel (HB), endcap (HB), outer (HO), and forward (HF) calorimeters. [31]

by Poisson statistics[1].

$$P_\mu(\nu) = e^{-\mu}\frac{\mu^\nu}{\nu!} \tag{2.1}$$

One can then solve for the mean number of collisions by counting the frequency in which there are no collisions:

$$P_\mu(\nu = 0) = e^{-\mu} \tag{2.2}$$

At low luminosities, the entire HF system simply counts the number of hits. At larger luminosities, there are too few events with no events ('zero starvation'), so HF is split into 864 independent segments ($\Delta\phi \times \Delta\eta = 0.175 \times 0.175$). Zero counting is

[1]It is actually an interesting aspect of Poisson statistics that by knowing only the mean number of collisions, one can solve for the instantaneous luminosity (Appendix C)

then done in each of these segments and then the information is combined to solve for the instantaneous luminosity.

The CMS experiment also makes use of the Pixel Luminosity Telescope in order to measure luminosity. These crystal diamond sensors not only give an estimate for the luminosity, but also locate the interaction point centroid. Furthermore, CMS calibrates these luminosities by measuring known $W\pm$ and Z^0 cross sections as well as measurements from the TOTEM experiment. This combined information determined the CMS recorded luminosity to within 2.5% systematic uncertainty and 0.5% statistical uncertainty in the 2012 dataset.

2.3.5 The Muon System

Though the tracker provides superior momentum resolution (particularly at low momentum where bending from the magnetic field is less pronounced), the muon system is important for several reasons. It allows muons to be cleanly identified as a track matching hits in the muon chamber (so called 'global muons' discussed in 4.6). The multiple layers of the muon system help to distinguish a real muon from a particle or jet of particles that has simply 'punched through' the calorimeters. Furthermore, the muon chambers are vital to the detector's ability to trigger on events with muons. The tracker alone would not be able to save such events for future processing in a timely manner. Finally, tracker and muon chamber information is combined for a superior position, momentum, and timing resolution than either subdetector would be able to accomplish individually.

The muon system consists of three types of subdetectors, drift tube (DT) chambers, cathode strip chambers (CSCs), and resistive plate chambers (RPCs). The muon system in the barrel region is outside of the solenoid magnet and intermingled with the magnet return yoke (Figure 2.8). CMS has also approved new Gas Electron

Multiplier (GEM) detectors to be installed during the second and third long LHC shutdowns. These new GEM detectors will be placed in the most forward parts of the muon system which have the highest rate and risk of saturation at future LHC luminosities [34].

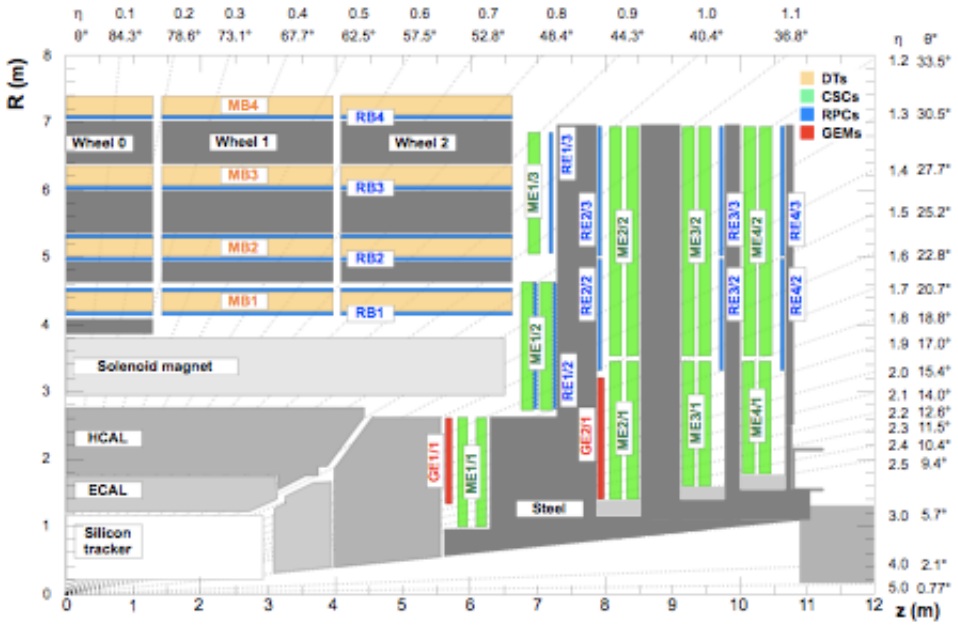

Figure 2.8: Layout of the CMS muon system showing the current locations of the DT (yellow), CSC (green), and RPC (blue) subdetectors as well as the future GEM subdetectors (red). [35]

2.3.6 Drift Tube Chambers

In the barrel of the CMS detector ($|\eta| < 1.2$), low muon flux, low neutron background flux, low magnetic field, yet large surface area make DT chambers the optimal choice. There are four layers of DT chambers nestled within the magnet return yoke at 4.0, 4.9, 5.9 and 7.0 meters from the beamline. Each layer is divided into 12, 30° segments. The segments are offset so that any muon will cross at least three of the

four DT layers. Each station is designed to give a position resolution of $100\mu m$ and a direction resolution of $1mrad$. Each DT chamber is coupled to 1 or 2 RPC chambers, further increasing the number of measured points for each muon and adding excellent time resolution.

2.3.7 Cathode Strip Chambers

In the two endcaps of the CMS detector ($0.9 < |\eta| < 2.4$), high muon flux, high neutron background flux, high magnetic field, yet smaller surface area make CSCs the optimal choice. As with the DT chambers, there are four layers of CSC chambers. Each station is divided into either 36 10° segments or 18 20° segments and is trapezoidal in shape. Each CSC chamber has six gas layers with radial cathode strips and almost perpendicular anode wires. As a muon showers in a CSC chamber, the position can be resolved by determining the centroid of the charge distribution on the cathode strips. The six layers allows for up to six coordinate measurements. Each chamber has a spacial resolution of $200\mu m$ and a direction resolution of $10mrad$.

2.3.8 Resistive Plate Chambers

The RPC detectors compliment both the DT and CSC detectors in the barrel and endcap regions, respectively. Though suffering from poor position resolution, RPCs have superior time resolution. Thus RPC information can better reconstruct proper bunch crossings. Furthermore, RPCs act as a complimentary muon trigger before the various subdetectors are able to combine information.

2.3.9 Gas Electron Multipliers

CMS is planning to add a first layer of GEM detectors during the second long shutdown planned for 2017-2018 [35, 36]. A second layer of GEM detectors is planned during the third long shutdown. These detectors will be a much needed addition for

a few reasons. GEM detectors are well suited to the high rates of the forward muon system (where they will be positioned) of the coming High Luminosity runs (see figure 2.2) without sacrificing excellent position resolution. Adding more muon stations to the forward muon system not only increases acceptance, but also helps with both triggering and rejection of backgrounds.

3. TRIGGER AND DATA

While taking data, CMS is capable of storing roughly 100 events per second for further processing and analysis. With collisions occurring every 50ns (2×10^7Hz) during 2011 and 2012 data collection, a timely and vast reduction in data is necessary without throwing away too many events of interest. This is the general problem of triggering on any experiment with such high rates. At CMS, the rate is first reduced from $\mathcal{O}(10^7\text{Hz})$ to $\mathcal{O}(10^4\text{Hz})$ by the Level-1 (L1) trigger using field-programmable gate arrays (FPGAs) and custom application-specific integrated circuits (ASICs). With much of the available decision time encompassed by the signal travel time, only $\mathcal{O}(1\mu\text{s})$ is available for computation and discrimination. At this first level, the tracker, calorimeters, and muon chambers have independent triggering systems. If an event is passed by one of these triggers, it is passed to the processor farm next to the detector cavern. This processor farm further refines the information from each subdetector and combines the information from various subdetectors for global triggers (see Figure 3.1). After passing the highest level triggering (HLT) algorithms, the event is moved to the LHC computing grid.

As different analyses desire triggering off different objects (muons, electrons/photons, jets, $\not\!\!E_T$, etc), CMS deploys a large number of independent triggers. Events collected from each type of object are stored in common Primary Datasets (PDs). The PD used in this study is SingleMu. As the name suggests, this is data collected by the single muon triggers. Our events are based off of the IsoMu24_eta2p1 HLT, which is seeded by SingleMu16er L1 trigger. The 'eta2p1' means that $|\eta|$ is restricted to 2.1, where both the muon and its $\Delta R < 0.5$ isolation cone are within tracking. Similarly the 'er' portion of the L1 seed name means that 'Eta is Restriced' to $|\eta| < 2.1$.

Figure 3.2 shows that the SiingleMu16 L1 trigger seed plateaus after a muon p_T of roughly 20 GeV. These events are fed into the IsoMu24 HLT whose efficiencies as a function of p_T and η can be seen in Figure 3.3. The bias from our trigger on the rate of our offline events is minimized by imposing an offline muon p_T cut of 30 GeV as will be discussed in section 5.1.

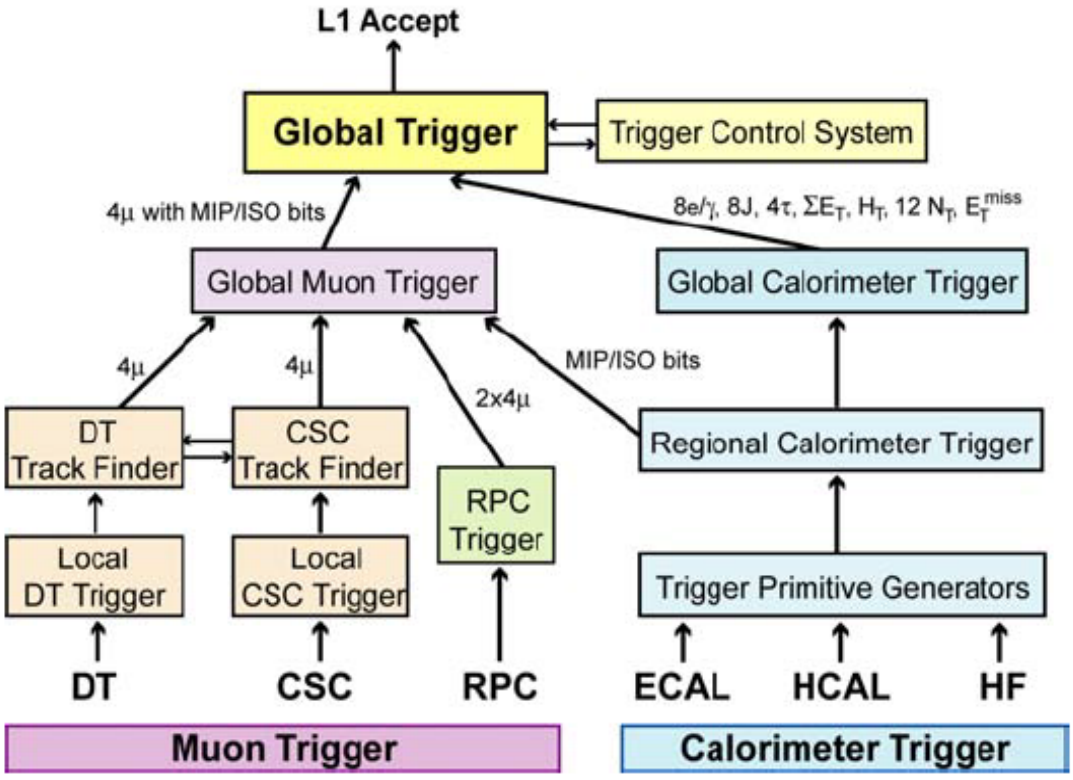

Figure 3.1: CMS trigger schematic of independent level-1 triggers of each subdetector combining information for the global high level triggers [31].

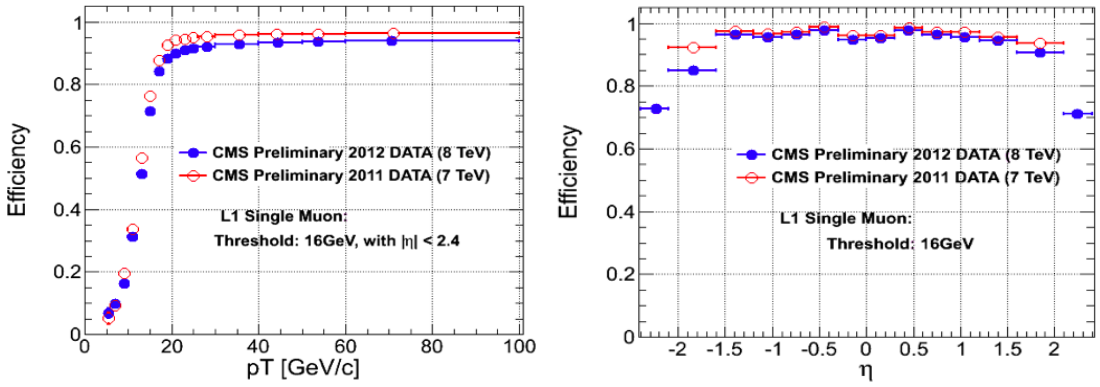

Figure 3.2: SingleMu16 L1 trigger seed efficiency as a function of p_T and η.

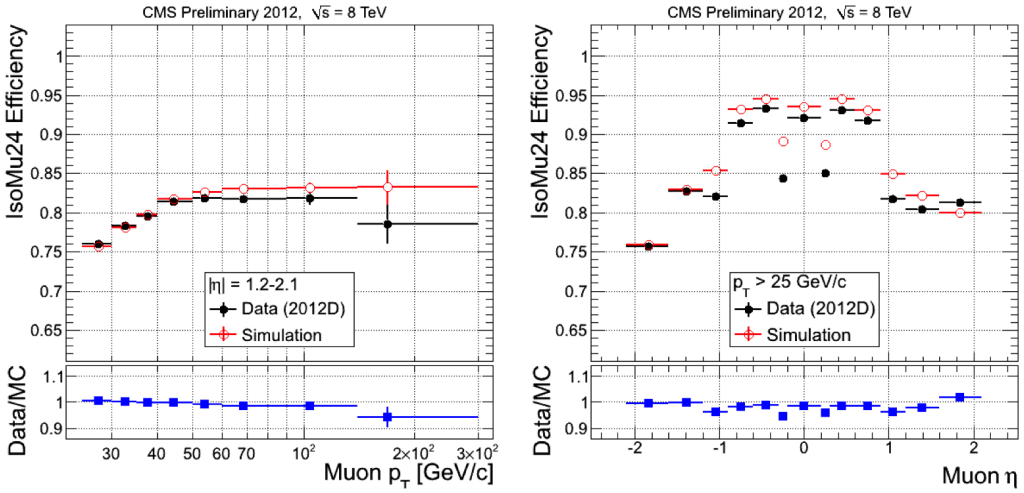

Figure 3.3: IsoMu24 HLT efficiency as a function of p_T and η [37]. Dips at $|\eta| \sim 0.2$ is due to cracks between DT wheels. Asymmetry in η is due to non-operational CSC chambers.

4. PHYSICS OBJECTS

4.1 The Particle Flow Algorithm

The particle flow algorithm makes use of the entire CMS detector to attempt to reconstruct each particle that hits our detectors. It does so with an iterative tracking algorithm which avoids double counting of any track/energy deposit [38]. First, hits in the muon chamber are matched to tracks in the inner tracker. The hits from these 'Particle-Flow Muons' are then removed from the event. Electron reconstruction then follows by combining tracks and ECAL deposits from the original electron itself as well as Bremsstrahlung photons and shower electrons. These hits are reconstructed using the Gaussian-Sum Filter, which is discussed in section 4.5. Once the 'Particle-Flow Electrons' are removed from the event, HCAL hits are matched to tracks in order to reconstruct 'Particle-Flow Charged Hadrons'. The mass and energy calibration given to these charged hadrons assumes them to be charged pions (with which the HCAL was calibrated). After these three types of particles have been removed (PF Muons, Electrons, and Charged Hadrons), 'Particle-Flow Photons and Particle-Flow Neutral Hadrons' are reconstructed. The photons are assumed to be any remaining ECAL deposits while the neutral hadrons are assumed to be any remaining HCAL deposits. The neutral hadrons are given the same mass and energy calibration as the charged hadrons.

The improved performance from the Particle Flow algorithm is one of the best strengths of the CMS experiment, but it can create some rare problems. In particular, we discovered that certain events with energetic hits at the edge of HCAL were giving large values for $\not\!\!E_T$. We discovered this to be energetic photons hitting the small region of HCAL which is uncovered by the ECAL. Since there was no associated

track or ECAL hit to these photons, the Particle Flow algorithm assumed them to be neutral pions. As such, energy calibrations for pions rather than photons were applied and the momentum balance of the system was disrupted. This is documented in [39].

4.2 Jets

Due to the strength of the QCD force, colored particles remain confined; that is colored particles pull quarks, antiquarks, and gluons out of the vacuum until a stable, color neutral configuration is reached. This process, known as hadronization, creates 'jets' of $\mathcal{O}(100)$ hadronic particles when quarks and gluons are created in high energy collisions. By summing the energy of these jets, we are able to approximate the original direction and momentum of the scattered parton.

Many jet clustering algorithms have been developed over the last 40 years [40]. For this analysis, we cluster individual particle flow constituents with the anti-k_t algorithm [41] using a clustering distance scale of $\Delta R = 0.5$. Though computationally expensive, the anti-k_t algorithm is chosen for both infrared and collinear safey.

4.3 $\not{E}_T$

Though an unfortunate name, the momentum imbalance within particle collisions is often referred to as 'missing transverse energy,' 'missing E_T,' or MET[1]. This momentum imbalance is quantified as the negative vector sum of each particle's transverse momentum (p_T) within the event:

$$\not{E}_{\mathrm{T}} = -\sum_{Objects} \vec{p_T^{\,i}} \tag{4.1}$$

[1]As energy is a scalar quantity, it has no direction and certainly no transverse component. Especially after reconstructing all subdetector hits as individual particles, we are no longer crudely applying a position vector to each energy deposit within our calorimeter. 'Missing transverse momentum' not only makes more sense mathematically and physically, but is also a more precise description of the quantity of interest.

The momentum imbalance is only calculated in the transverse direction since the scattering partons are not likely to have balancing momenta along the beamline (as they share this 4 TeV of momentum with all other partons). To a good approximation, the net momentum in the transverse direction of the colliding partons is negligible. Therefore, we can assume conservation of momentum and look for large $\not{E}_{\mathrm{T}}$ as a probe for events with neutrinos, dark matter particles, or any other particle which is not captured by our detector.

4.4 Photons

Both photons and electrons (next section) depend heavily on clustering and supercluster within the ECAL. Since photons will convert into electron-positron pairs as they pass through material before the ECAL and electrons give off bremsstrahlung radiation (which can, in turn, produce more electron-positron pairs) before reaching the ECAL, both objects can appear as a mixed shower of photons and electrons. Due to bending from the magnetic field, the electrons and positrons (and their respective showers) are bent in the azimuthal (ϕ) direction. 97% of the energy of each individual electron/photon is captured in a 5x5 crystal 'cluster'. Summing these clusters in the ϕ direction derives the supercluster of our electromagnetic object. For both electrons and photons, a reconstructed position is derived from the energy-weighted mean position of the supercluster. Photons can be somewhat distinguished from electrons by their larger penetration depth.

Photon identification makes use of information from the tracker, ECAL, and HCAL. From the tracker, the number and total energy of tracks are summed within an isolation cone. This helps to reject hadronic jets as well as single charged hadrons. The ECAL is used not only to reconstruct the photon energy, but also to reduce backgrounds. Chiefly, π^0's (which decay to two photons) can be rejected by considering

shower shape variables such as the E_T around the supercluster and the R_9 variable, which is the ratio of energy contained in a 3x3 array of crystals divided by the total supercluster energy. The fine granularity of the ECAL can also distinguish photons which don't originate from the primary vertex. The HCAL can then reject charged hadrons which didn't leave sufficient tracks as well as neutral hadrons which survive to the HCAL. The most common isolation variable of this sort is the HCAL energy divided by the ECAL energy ('H/E') for the tower at the center of the supercluster. In CMS these variables are further optimized and combined by using a neural net. No specific identification benchmark is given here since photons are not considered in this analysis.

4.5 Electrons

As with photons, information is combined from the tracker, ECAL, and HCAL to determine quality electrons. The main difference from photons is that electrons should have exactly one high quality track coming directly from the primary vertex matched to the electromagnetic cluster. Electron reconstruction therefore has the additional burden of reconstructing a track as the electron gives off bremsstrahlung radiation at various points on its path to the ECAL. Since electron reconstruction depends on tracking information, this also limits electron reconstruction to be within the fiducial tracking volume ($|\eta| < 2.5$). Though track parameters vary in a non-Gaussian manner (as a function of electron momentum) as the electron passes through various layers of material, the fluctuations from each layer of material can be roughly approximated as gaussian. These gaussian fluctuations can be propagated from each layer to the next. This is known as the Gaussian Sum Filter [42]. This algorithm allows tracking parameters and their errors to be recursively calculated along the full electron trajectory. This also allows electrons to be classified based on

the amount of bremsstrahlung radiation given off from the innermost to outermost layer of the tracker. The energy measurements from the tracker and the ECAL nicely complement one another since tracker momentum resolution degrades with energy while ECAL energy resolution improves with energy. The tracker momentum measurement and uncertainty will hereafter be denoted as 'p' while the ECAL energy measurement will be denoted as 'E'. When these two measurements roughly agree ($|E/p - 1| < 2\sigma_{E/p}$), the final energy is taken as the weighted average of both. If the ECAL supercluster energy greatly exceeds the tracker momentum ($E/p > 1 + 2\sigma_{E/p}$), it is assumed that the tracker underestimated the momentum and the ECAL energy alone is used. If the ECAL supercluster energy is much less than the tracker momentum ($E/p < 1 - 2\sigma_{E/p}$), then it is uncertain whether there was an underestimate by the ECAL or an overestimate by the tracker. In this case, the tracker measurement is taken for $E < 15$GeV and the ECAL measurement is taken for $E > 15$GeV (where the two subdetectors have better resolution, respctively).

After electron energy has been measured, determining their proper identification is as follows: A geometrical matching is applied between the tracker and the electromagnetic supercluser in both the η and ϕ directions (so called $|\Delta\eta_{in}|$ and $|\Delta\phi_{in}|$, respectively). The specific cut values are given in Table 4.1. A shower shape variable ($\sigma_{\eta\eta}$) is used to quantify the spread in the electron energy in the η direction.

$$\sigma_{\eta\eta} = \sum_{Crystals} (\eta_i - \eta_s)^2 \frac{E_i}{E_s} \tag{4.2}$$

where we sum over the 'i'-th crystal of the ECAL supercluster and 's' is the seed cluster [43]. This variable is helpful for both distinguishing electrons from jets and also to classify the amount of bremsstrahlung radiation which the electron has given off. Next, the HCAL energy divided by the ECAL energy ('H/E') for the tower at the

center of the supercluster is used to distinguish our electron from charged hadrons as is done with photons. Then the ECAL energy, E, and the track momentum, p, are required to be relatively consistent (actually $1/E$ and $1/p$ are compared as this has been seen to give the best performance). Furthermore, at least one hit within the inner tracker (before a photon is likely to have produced an electron-positron pair) to distinguish this electromagnetic cluster from that of a photon. Finally, isolation is applied with all particle flow particles within a cone of $\Delta R < 0.4$. Our full electron ID is summarized in Table 4.1. Slightly different cuts are used between the barrel and endcap regions to maximize performance. Our identification criteria chosen here is referred to as the CMS GSF tight electron working point.

Criteria	EB	EE
$\lvert\Delta\eta_{in}\rvert <$	0.004	0.005
$\lvert\Delta\phi_{in}\rvert <$	0.03	0.02
$\sigma_{\eta\eta} <$	0.01	0.03
$H/E <$	0.12	0.10
$\lvert 1/E - 1/p\rvert <$	0.05	0.05
$N^{track}_{inner} \geq$	1	1
$(\Sigma^{\Delta R<0.4}_{photons} E_T)/(E^e_T) <$	0.15	0.10
$(\Sigma^{\Delta R<0.4}_{ChargedHadrons} E_T)/(E^e_T) <$	0.05	0.05
$(\Sigma^{\Delta R<0.4}_{NeutralHadrons} E_T)/(E^e_T) <$	0.10	0.10

Table 4.1: Electron identification criteria. EB and EE designate the cut values in the barrel and endcap regions, respectively.

4.6 Muons

Muons are reconstructed using information from both the tracker and the muon chambers. As noted previously, the tracker gives the best momentum resolution, while the muon chambers are vital to the successful triggering of muon events. Both

subsystems are crucial to the final reconstruction and overall purity of reconstructed muons. During muon reconstruction at Level-1 and Level-2 triggering, only information from the muon chambers is used while assuming the nominal interaction point. At the High Level Triggering and subsequent full reconstruction, both the tracker and muon chambers are used with the interaction point no longer fixed. A χ^2 fit is used throughout this reconstruction to determine the quality of the muon track and suggest outlying hits. This χ^2 fit always considers bremsstrahlung radiation and energy loss from the various materials between the tracker and muon system (electromagnetic and hadronic calorimeters as well as magnet and support structure).

Compared to other types of reconstructed particles, muons are fairly simple due to their long lifetime and radiation lengths. This is why muons are the first type of particle to be reconstructed and taken out of the event by the particle flow algorithm (4.1). This is also why muons provide such a clean signature within the CMS detector. All muons used for analysis hereafter will be muons reconstructed by the particle flow algorithm ('PF muons'). They will be required to have at least 10 tracker hits with at least one of these hits being in the pixel tracker. At least two muon chambers must have matching segments. The χ^2 fit normalized by the number of hits must be less than 10. The reconstructed vertex must be within $2mm$ of the beamline. Finally, certain isolation cuts are made as described in the next paragraph. Our full muon ID is summarized in Table 4.2.

As discussed in the previous section on electrons, light leptons are commonly produced in the showering of hadrons, particularly c and b type hadrons. As a result, we make isolation cuts to discriminate these secondary leptons from those produced more cleanly and directly. We apply CMS recommended 'loose PF combined relative isolation' which amounts to summing the E_T of PF hadrons (both charged and neutral) and photons within a cone of $\Delta R < 0.4$ and dividing by the muon p_T. $\Delta\beta$

Criteria
Global μ
Number of tracker hits > 10
Number of (pixel) tracker hits > 1
Muon chambers with matching segments > 2
$\chi^2/N < 10$
$\sigma_{xy} < 2$mm
$(\Sigma^{\Delta R<0.4}_{photons,hadrons} E_T)/(p^{\mu}_T) < 0.2$

Table 4.2: Muon identification criteria.

corrections are applied to compensate for pileup contamination.

4.7 Hadronic Taus

Unlike electrons and muons, tau leptons are heavy enough to decay into hadrons. This occurs roughly 60% of the time, while the tau will decay to lighter leptons roughly 40% of the time. Experimentally, hadronic taus can be quite difficult since their hadronic jets can look quite similar to typical QCD processes which have cross sections several orders of magnitude larger. Of course, only hadronic taus need to be reconstructed as leptonic taus will present themselves in the electron and muon final states (along with missing momentum from the neutrinos.)

The most common criteria for identifying hadronic taus within CMS is the Hadrons Plus Strips (HPS) algorithm. Due to conservation of tau charge, our decay products must include an odd number of charged hadrons, mainly pions. The neutral components of the decay, mainly π^0's, quickly decay to photons. These photons create several electron and positron pairs. As these electrons and positrons are bent in different directions in ϕ, this forms an azimuthal strip of energy in the ECAL. Thus the 'Hadrons' plus 'Strips' refers to the charged and neutral component of the tau decay.

Though hadronic taus are not a focus of this thesis, all hadronic taus subsequently

refered to are required to be 'single prong.' This means we are focused on tau decays to a single charged pion in order to minimize QCD background contamination. They are also required to pass Loose MVA isolation as documented in [44]

4.8 Bottom-Tagged Jets

Due to the longer lifetimes of bottom-type mesons ($\mathcal{O} \sim 10^{-12}$s), they travel on the order of a milli-meter before decaying. Given the fine resolution of the CMS tracker, a 'secondary vertex' can often be reconstructed. There are many b-tagging algorithms within CMS. This analysis makes use of the Combined Secondary Vertex (CSV) algorithm which uses a neural net to combine the distance from the primary vertex to the secondary vertex, the invariant masses of the jet constituents (to reject contamination from long-lived mesons, the direction of the vertices compared to the jet direction, the number of tracks stemming from the secondary vertex, the energy stemming from the secondary vertex versus all tracks within the jet, and various other quantities [45].

There are multiple benchmark points for the CSV algorithm. The two benchmark points of interest to this analysis are the medium (CVSM) and tight (CSVL) points with a b-tagging efficiency of roughly 70% and 85% and a jet mis-tag rate of 1.5% and 10%, respectively. Our analysis requires 0 CSVL b-jets, which is the more restrictive benchmark between the two points. This benchmark is chosen for multiple reasons. The first is that this more severely reduces our largest background, $t\bar{t}$. The other reason is that b-tagging only takes place within tracking coverage. As our signal often consists of very forward jets, this mis-tagging rate does not significantly reduce our signal.

4.9 Weak Boson Fusion

Weak/Vector Boson Fusion (WBF/VBF) processes were originally devised for heavy Higgs Boson searches using the Superconducting Supercollider [46][47][48]. As WBF cross sections fall off slower than direct production as a function of collision energy, WBF is increasingly sensitive as energy increases. see Figure 4.1. WBF has the unique signature of two forward jets (emanating from the quarks which radiated the fusing bosons) with high transverse momentum (p_T), large separation in pseudorapidity ($\Delta\eta$), and a large di-jet invariant mass (m_{jj}). Furthermore, the decay products of our heavy particles are found cleanly within the central region between our WBF jets. Furthermore, WBF jets do not achieve this large p_T and m_{jj} unless producing a heavy particle. Hence backgrounds from SM particles with lighter masses rarely imitate these kinematics. With the discovery of the 125 GeV Higgs-like Boson, WBF is now heavily employed by many groups within CMS and ATLAS. Only more recently has the community started to fully realize the potential of these processes in SUSY searches [21].

Figure 4.2 shows that we expect a signal cross section (O)(1-10)fb^{-1} for moderate gaugino masses. Figure 4.3 illustrate the signal discrimination power of WBF kinematic variables while Figure 4.4 shows significance ($\frac{S}{\sqrt{S+B}}$) as a function of our selection thresholds. It is also important to realize that there is a direct correlation between our WBF kinematic variables m_{jj}, $\Delta\eta$, and p_T (see Appendix A).

4.10 Monte Carlo Simulation

Since many aspects of a proton-proton collision are probabilistic in nature, from which partons of each proton interact, which particles are produced, and how those particles interact with the detector, one can never know a priori how the event will unfold. We can measure the probabilities of all of the above to high precision and

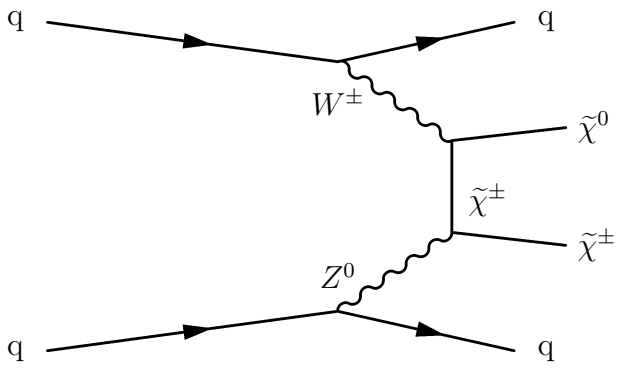

Figure 4.1: WBF production of a neutralino and chargino from $W^{\pm}Z^0$ fusion.

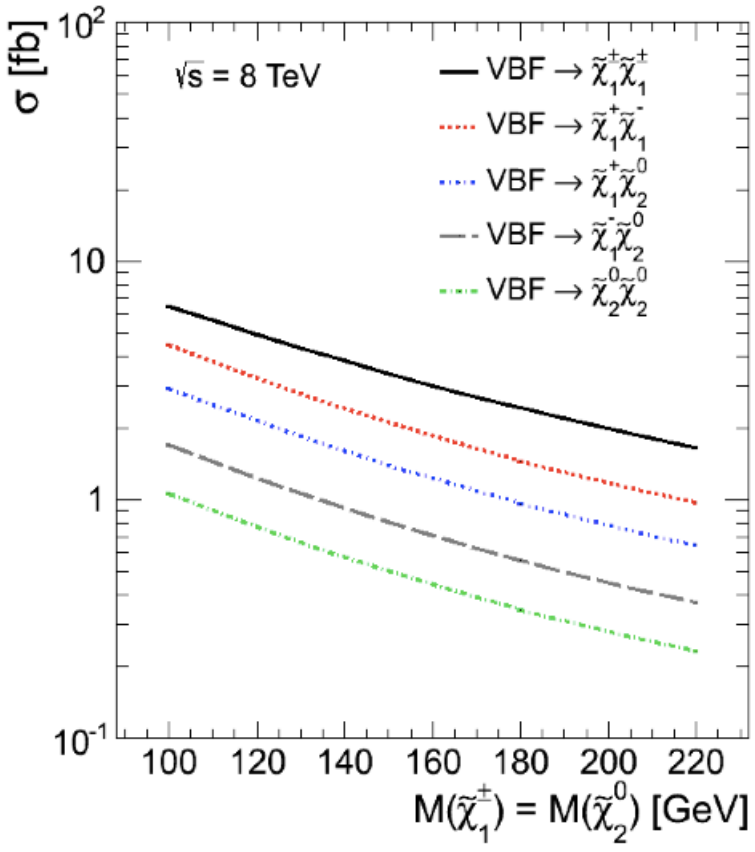

Figure 4.2: Cross section of WBF gaugino production such as Figure 4.1. $\widetilde{\chi_1^{\pm}\chi_1^{\pm}}$ has the largest cross section due to the larger combinatorics of having two up or down quarks scatter versus one up quark and one down quark.

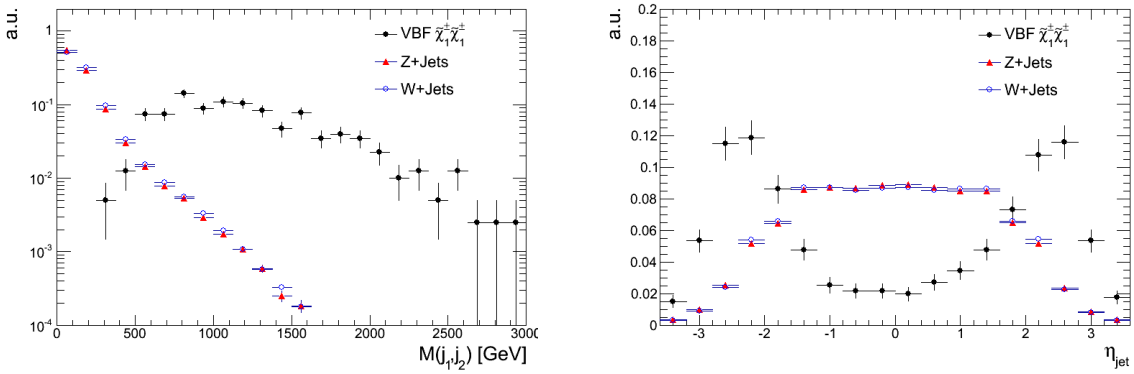

Figure 4.3: Dijet invariant mass (left) and jet pseudorapidity for a WBF signal benchmark point (black), Z + jets (red) and W + jets (blue).

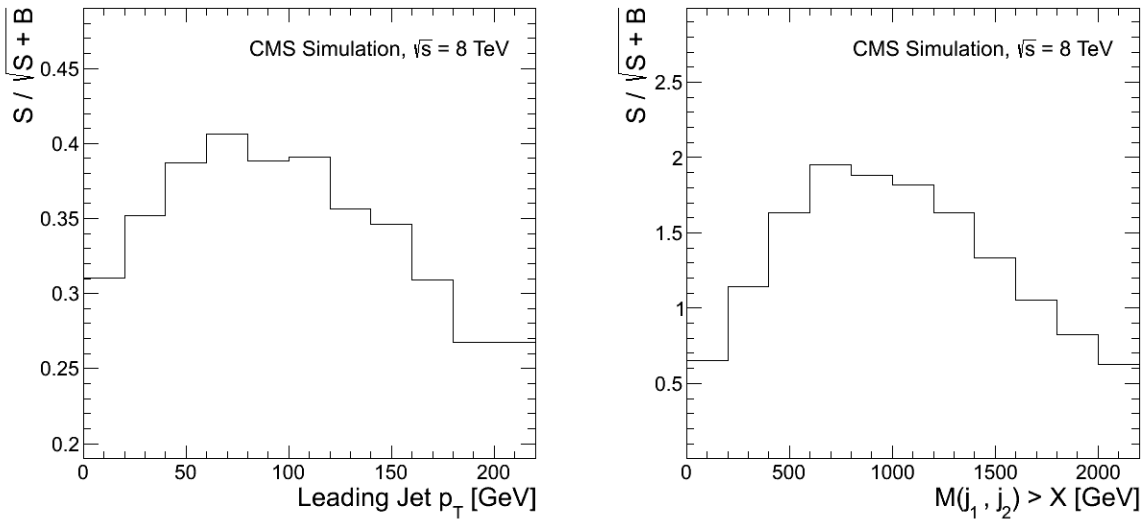

Figure 4.4: Significance versus leading jet p_T cut (left) and dijet invariant mass cut (right) for a WBF signal benchmark point.

figure out the probability for each outcome. Given a large number of collisions, the overall distributions can be simulated at an incredible degree of precision.

The parton-level interaction is simulated by MadGraph 5 [55]. The subsequent hadronization as well as initial and final state radiation is done by Pythia 6 [56]. The detector simulation is performed by Geant4 [57] within the CMS software framework. CTEQ 6.6 was used as the parton distribution function [59].

This thesis will limit its focus to 'WBF jets plus two lepton' final states. Our intended signal is WBF-produced electro-weak SUSY (EWKino) particles. Figure 5.1 and Figure 5.2 display archetypal decays of EWKino particles. The decays shown here are for illustration and certainly not an exhaustive list. By looking for two or more leptons our final state could contain $\widetilde{\chi}_2^0\widetilde{\chi}_0^0$ production where both leptons emanate from the $\widetilde{\chi}_2^0$ or $\widetilde{l^+}\widetilde{l^-}$ production where each slepton produces one lepton. By considering the combinatorics of various initial states and decays, we arrive at numerous possible combinations of lepton pairs in our final state (like-sign same-flavor, opposite-sign different-flavor, etc.)

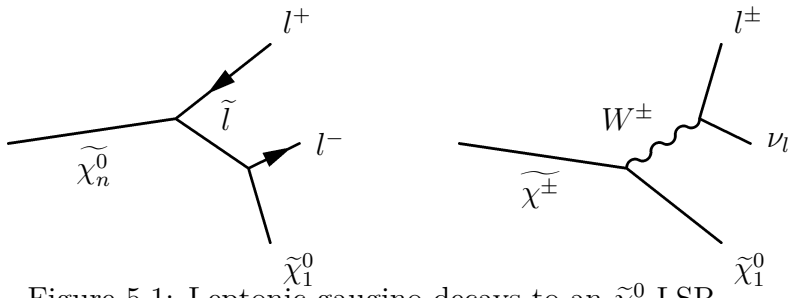

Figure 5.1: Leptonic gaugino decays to an $\widetilde{\chi}_1^0$ LSP.

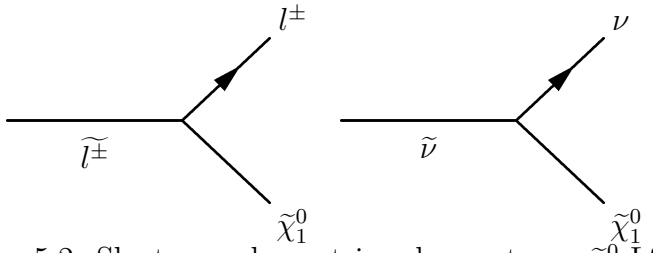

Figure 5.2: Slepton and sneutrino decays to an $\widetilde{\chi}_1^0$ LSP.

In order to be sensitive to a maximum number of possible signals, this search is divided among all possible combinations of two lepton final states (e^+e^-, $e^\pm e^\pm$, $e^\pm\mu^\mp$, $e^\pm\mu^\pm$, $e^\pm\tau_h^\mp$, $e^\pm\tau_h^\pm$, $\mu^+\mu^-$, $\mu^\pm\mu^\pm$, $\mu^\pm\tau_h^\mp$, $\mu^\pm\tau_h^\pm$, $\tau_h^+\tau_h^-$, $\tau_h^\pm\tau_h^\pm$) where e, μ, and τ_h denote electrons, muons, and hadronic taus, respectively. This thesis will focus on the $e^\pm\mu^\mp$ and $e^\pm\mu^\pm$ channels.

5.1 Trigger

All muon final states, including $e\mu$ make use of muon triggering due to the higher efficiency and lower p_T threshold as compared to other lepton triggers (Table 5.1). In particular, $e\mu$ is based off of HLT_IsoMu24_eta2p1, which requires an isolated muon with a p_T of 24 GeV or more within an $|\eta|$ of 2.1. Since CMS tracking extends to $|\eta| \sim 2.4$, the $|\eta| < 2.1$ requirement places both the muon and $\Delta R = 0.5$ isolation cone within this range. Our offline muon selection requires a p_T of 30 in order to prevent trigger thresholds from affecting the observed rate.

Channel	Trigger
eτ_h, ee	HLT_Ele27_WP80
$\mu\tau_h$, $\mu\mu$, eμ	HLT_IsoMu24_eta2p1
$\tau_h\tau_h$	HLT_DoubleMediumIsoPFTau35_Trk1_eta2p1_Prong1

Table 5.1: High level triggers across all search channels

The HLT_IsoMu24_eta2p1 is the trigger with the lowest p_T threshold to remain unprescaled for all 2012 8TeV runs (2012A-2012D).

5.2 Offline Event Selection

As already noted, the $e\mu$ channels use events firing the HLT_IsoMu24_eta2p1 trigger and requires an isolated muon with offline p_T cut of 30 GeV and $|\eta| < 2.1$. The

electron, being free of trigger bias, is allowed a softer p_T cut of 15 GeV. The "Tight" identification working points are used for both leptons as documented in sections 4.5 and 4.6. We require $\not{E}_{\mathrm{T}} > 75$ GeV to magnify the signature of a potential dark matter particle. Since $t\bar{t}$ is our dominant background, the Loose CSV working point is used for our b-jet veto. The large background rejection in this case greatly outweighs the increased mistagging rate. Only jets with p_T greater than 20 GeV and separated from the leptons in the eμ pairs by $\Delta R > 0.3$ are searched for b-tags. Finally, we require two VBF-tagged jets ($p_T^{jets} > 50$ GeV, $m_{jj} > 250$ GeV, $|\Delta\eta| > 4.2$, and $\eta_1 \cdot \eta_2 < 0$). Cut-flow tables for our backgrounds are given in Table 5.2 for OS and Table 5.3 for LS.

OS						
Background	Trigger	μ	e	$e\mu + 0b$	$\not{E}_{\mathrm{T}}$	Signal
$t\bar{t}$	6.1×10^{5}	5.2×10^{5}	5.5×10^{4}	5.4×10^{3}	1.8×10^{3}	22.8 $\pm_{stat}$ 3.9
$Z \to \tau\tau$	6.2×10^{5}	3.1×10^{5}	1.5×10^{4}	1.3×10^{4}	3.5×10^{2}	2.6 $\pm_{stat}$ 1.5
$Z \to \mu\mu$	1.3×10^{7}	1.2×10^{7}	1.5×10^{4}	8.8×10^{3}	5.9×10^{1}	1.1 $\pm_{stat}$ 1.1
$Z \to ee$	9.4×10^{1}	2.5×10^{1}	2.2×10^{1}	1.5×10^{1}	2.0×10^{0}	0 $+_{stat}$ 0.99
$W \to l\nu$+jets	9.5×10^{7}	7.2×10^{7}	3.7×10^{4}	1.1×10^{4}	6.4×10^{2}	3.8 $(\pm^{2.9}_{2.2})_{stat}$
WW	1.2×10^{5}	9.7×10^{4}	7.6×10^{3}	6.5×10^{3}	6.9×10^{2}	2.31 $\pm_{stat}$ 0.64
WZ	7.2×10^{3}	6.4×10^{3}	1.6×10^{3}	9.2×10^{2}	1.3×10^{2}	0.467 $\pm_{stat}$ 0.078
$ZZ \to ll\nu\nu$	3.5×10^{3}	3.2×10^{3}	1.6×10^{1}	1.1×10^{1}	2.6×10^{0}	0 $+_{stat}$ 0.028
$ZZ \to llll$	1.2×10^{3}	1.0×10^{3}	3.1×10^{2}	2.1×10^{2}	4.0×10^{0}	0.0047 $\pm_{stat}$ 0.0027
W^+W^+qq	5.4×10^{2}	4.8×10^{2}	3.7×10^{1}	6.9×10^{-1}	3.0×10^{-1}	0 $+_{stat}$ 0.050
W^-W^-qq	2.0×10^{2}	1.7×10^{2}	1.4×10^{1}	2.3×10^{-1}	1.1×10^{-1}	0 $+_{stat}$ 0.018
$H \to \tau\tau$	2.0×10^{2}	1.5×10^{2}	9.8×10^{0}	7.0×10^{0}	1.2×10^{0}	0.258 $\pm_{stat}$ 0.018
$H \to WW$	1.9×10^{2}	1.5×10^{2}	2.8×10^{1}	2.0×10^{1}	4.4×10^{0}	0.826 $\pm_{stat}$ 0.045
$H \to ZZ \to ll\nu\nu$	7.2×10^{0}	6.1×10^{0}	3.1×10^{-2}	1.7×10^{-2}	4.9×10^{-3}	0.00056 $\pm_{stat}$ 0.00025
$H \to ZZ \to llll$	1.2×10^{1}	1.1×10^{1}	2.7×10^{0}	1.4×10^{0}	1.4×10^{-2}	0.00139 $\pm_{stat}$ 0.00098

Table 5.2: MC-based cut-flow table for various backgrounds in the OS $e\mu$ final state.

The dominant background is $t\bar{t}$ due to the presence of real $e\mu$ pairs, missing momentum (from neutrinos) and large jet multiplicity for the VBF cuts. Diboson pairs and $Z \to \tau\tau$ are also able to produce real $e\mu$ pairs, but only represent 8%

LS						
Background	Trigger	μ	e	$e\mu + 0b$	$\not{E}_{\mathrm{T}}$	Signal
$t\bar{t}$	6.1×10^{5}	5.2×10^{5}	5.5×10^{4}	1.0×10^{3}	2.7×10^{2}	$2.0 \pm_{stat} 1.2$
$Z \to \tau\tau$	6.2×10^{5}	3.1×10^{5}	1.5×10^{4}	1.8×10^{2}	1.4×10^{1}	$0 +_{stat} 0.85$
$Z \to \mu\mu$	1.3×10^{7}	1.2×10^{7}	1.5×10^{4}	3.5×10^{3}	2.1×10^{1}	$0 +_{stat} 1.1$
$Z \to ee$	9.4×10^{1}	2.5×10^{1}	2.2×10^{1}	1.6×10^{1}	1.0×10^{0}	$0 +_{stat} 0.99$
$W \to l\nu$+jets	9.5×10^{7}	7.2×10^{7}	3.7×10^{4}	6.6×10^{3}	4.2×10^{2}	$0 +_{stat} 2.7$
WW	1.2×10^{5}	9.7×10^{4}	7.6×10^{3}	8.6×10^{1}	1.0×10^{1}	$0 +_{stat} 0.20$
WZ	7.3×10^{3}	6.4×10^{3}	1.6×10^{3}	9.4×10^{2}	1.3×10^{2}	$0.93 \pm_{stat} 0.11$
$ZZ \to ll\nu\nu$	3.5×10^{3}	3.2×10^{3}	1.6×10^{1}	1.1×10^{0}	2.5×10^{-1}	$0 +_{stat} 0.028$
$ZZ \to llll$	1.2×10^{3}	1.0×10^{3}	3.1×10^{2}	2.1×10^{2}	4.0×10^{0}	$0.0063 \pm_{stat} 0.0031$
$W^{+}W^{+}qq$	5.4×10^{2}	4.8×10^{2}	3.7×10^{1}	2.3×10^{1}	1.0×10^{1}	$0.61 \pm_{stat} 0.18$
$W^{-}W^{-}qq$	2.0×10^{2}	1.7×10^{2}	1.4×10^{1}	8.8×10^{0}	3.6×10^{0}	$0.18 \pm_{stat} 0.06$
$H \to \tau\tau$	2.0×10^{2}	1.5×10^{2}	9.8×10^{0}	2.1×10^{-1}	3.1×10^{-2}	$0 +_{stat} 0.0014$
$H \to WW$	1.9×10^{2}	1.5×10^{2}	2.8×10^{1}	1.7×10^{-1}	3.7×10^{-2}	$0 +_{stat} 0.0025$
$H \to ZZ \to ll\nu\nu$	7.2×10^{0}	6.1×10^{0}	3.1×10^{-2}	6.5×10^{-3}	1.1×10^{-3}	$0.00011 \pm_{stat} 0.00011$
$H \to ZZ \to llll$	1.2×10^{1}	1.1×10^{1}	2.7×10^{0}	1.4×10^{0}	1.8×10^{-2}	$0.0042 \pm_{stat} 0.0017$

Table 5.3: MC-based cut-flow table for varios backgrounds in the LS $e\mu$ final state.

and 7% (based on MC) of the total OS background contribution to the signal region respectively as they suffer from much smaller cross sections and/or jet multiplicity. Diboson pairs play a larger role in the LS channel, where they constitute almost half of the signal region prediction (based on MC), while the DY + jets contribution is negligible. $W \to l\nu$ is an important background when one lepton can be faked due to its large cross section and missing momentum from a neutrino. However, $W \to l\nu$ + jets only represents 11% of the background contribution to the signal region (according to MC). QCD is negligible due to the large $\not{E}_{\mathrm{T}}$ cut as well as low j$\to l$ fake rates for l =e,μ.

5.3 Data-Driven Background Estimation

As $t\bar{t}$ is the dominant background for both opposite and like-sign final states, $t\bar{t}$ deserves the most extensive data-driven background estimation strategy. Our subdominant backgrounds will also have data-driven elements, minimizing our dependence on simulation. Negligible backgrounds are taken directly from simulation

(with systematic uncertainties applied).

5.3.1 $t\bar{t}$ Background Estimation

The major problem of background estimation is estimating our contamination to the signal region without looking at actual signal events, hence biasing our selections. And yet, depending solely on simulation is also problematic. The optimal balance is achieved by defining sets of cuts which are similar, yet orthogonal, to our signal region and have a high purity of the background of interest. The $t\bar{t}$ background estimation makes use of four such 'control regions' to extrapolate to the signal region without biasing our selection.

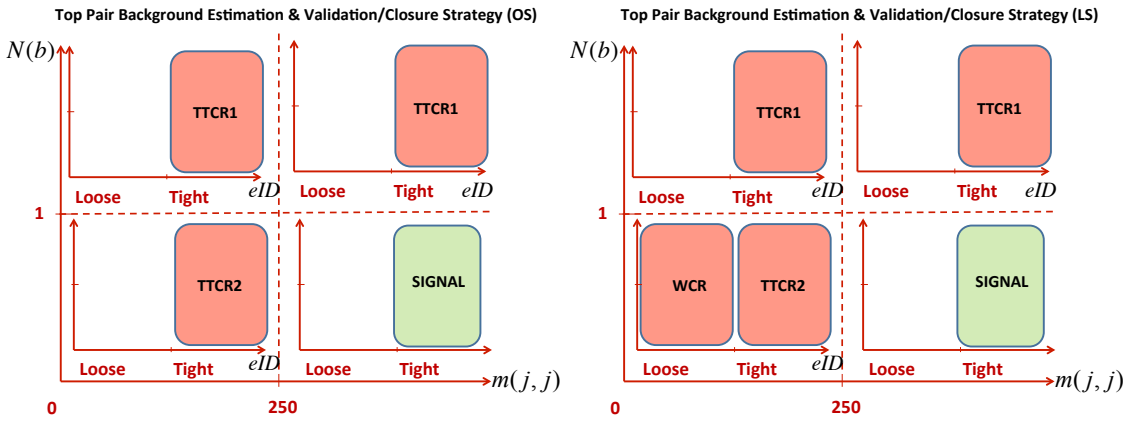

Figure 5.3: Schematics of the four control regions used for $t\bar{t}$ opposite-sign (left) and like-sign (right) background estimation. 'WCR' in the LS diagram denotes a control region for $W \to l\nu$ + jets which will be discussed in the next section.

Both opposite and like-sign employ two control regions as can be see in Figure 5.3. To move from our signal region to control region 1 (CR1), the $|\Delta\eta|$ and m_{jj} requirements are dropped and events are required to have 1 b-tagged jet (instead of 0 b-tagged jets in the signal region) to increase $t\bar{t}$ purity and avoid signal region

contamination. To move from our signal region to control region 2 (CR2), events satisfying the VBF selections are rejected. To extrapolate to the signal region, the $t\bar{t}$ rate obtained from CR2 (Data minus non-$t\bar{t}$ MC) is corrected/multiplied by the VBF cut efficiency (ϵ_{VBF}^{Data}) measured from CR1 (see Equation 5.1). The same definition and strategy is used in both OS and LS eμ channels. Plots of all four $t\bar{t}$ control regions can be found in Figures 5.4 and 5.5. The VBF cut efficiencies measured from data and MC are given in Tables 5.4 and 5.5 for the OS and LS channels, respectively. The $t\bar{t}$ statistics and purity are lower in CR2 due to the b-jet veto (see Tables 5.6 and 5.7 for the OS and LS channels respectively.) Loosening electron identification criteria allows like-sign CR2 to become a $W \rightarrow l\nu$ control region. This allows the contamination in CR2 to be better constrained. A summary of the final numbers used for estimation is in Table 5.8.

$$N_{Signal}^{t\bar{t}} = (N_{CR2}^{data} - N_{CR2}^{\neq t\bar{t}MC}) \times \epsilon_{VBF}^{Data} \tag{5.1}$$

5.3.2 $W \rightarrow l\nu$ + jets Background Estimation

The $W \rightarrow l\nu$ + jets background almost always results from a real prompt muon with a fake electron due to the larger j→e fake rate. As this fake electron is charge-blind, $W \rightarrow l\nu$ has similar yields for OS and LS. As stated in the previous section, although the $W \rightarrow l\nu$ + jets contribution to the signal region is only roughly 10%, there is an important level of contamination from $W \rightarrow l\nu$ + jets in $t\bar{t}$ CR2. We can obtain a semi-clean $W \rightarrow l\nu$ + jets control region by requiring electrons to pass the Loose identification working point but not the Tight criteria, while remaining orthogonal to the $t\bar{t}$ control regions and signal region. The kinematics of this control region are given in Figure 5.6. Using this control region, we obtain a data-to-MC scale factor of 1.118 $(\pm^{0.162}_{0.415})_{stat}$ $(\pm^{0.043}_{0.040})_{lumi}$ (see Table 5.9). This scale factor allows

OS		
Background	CR1 Expectation	CR1 Expectation ($m_{jj} > 250$)
$t\bar{t}$	6317.2 $\pm_{stat}$ 65.4	107.7 $\pm_{stat}$ 8.5
$Z \to \tau\tau$	141.3 $\pm_{stat}$ 10.9	1.7 $\pm_{stat}$ 1.2
$Z \to \mu\mu$	13.8 $\pm_{stat}$ 4.0	0 $+_{stat}$ 1.1
$Z \to ee$	0 $+_{stat}$ 1.0	0 $+_{stat}$ 1.0
$W \to l\nu + 0jets$	0 $+_{stat}$ 41.9	0 $+_{stat}$ 41.9
$W \to l\nu + 1jets$	0 $+_{stat}$ 6.0	0 $+_{stat}$ 6.0
$W \to l\nu + 2jets$	15.4 $\pm_{stat}$ 5.1	0 $+_{stat}$ 1.7
$W \to l\nu + 3jets$	34.3 $\pm_{stat}$ 5.6	0.9 $\pm_{stat}$ 0.9
$W \to l\nu + 4jets$	52.6 $\pm_{stat}$ 8.2	0 $+_{stat}$ 1.3
WW	76.3 $\pm_{stat}$ 3.7	0.5 $\pm_{stat}$ 0.3
WZ	26.0 $\pm_{stat}$ 0.6	0.29 $\pm_{stat}$ 0.06
$ZZ \to ll\nu\nu$	0.5 $\pm_{stat}$ 0.1	0.03 $\pm_{stat}$ 0.03
$ZZ \to llll$	1.19 $\pm_{stat}$ 0.04	0.0126 $\pm_{stat}$ 0.004
W^+W^+qq	0.3 $\pm_{stat}$ 0.1	0.05 $\pm_{stat}$ 0.05
W^-W^-qq	0.02 $\pm_{stat}$ 0.02	0 $+_{stat}$ 0.02
$H \to \tau\tau$	0.41 $\pm_{stat}$ 0.02	0.08 $\pm_{stat}$ 0.01
$H \to WW$	1.58 $\pm_{stat}$ 0.06	0.29 $\pm_{stat}$ 0.03
$H \to ZZ \to ll\nu\nu$	0.0016 $\pm_{stat}$ 0.0004	0.0001 $\pm_{stat}$ 0.0001
$H \to ZZ \to llll$	0.012 $\pm_{stat}$ 0.003	0.003 $\pm_{stat}$ 0.001
Total MC	6680.9 $\pm^{79.6}_{67.5}$	111.5 $\pm^{43.2}_{8.7}$
Purity	94.6%	96.5%
Data	6775	84
SF	1.015 $(\pm^{0.016}_{0.018})_{stat}$ $(\pm^{0.033}_{0.031})_{lumi}$	0.744 $(\pm^{0.105}_{0.407})_{stat}$ $(\pm^{0.024}_{0.022})_{lumi}$
ϵ^{Data}_{VBF}	$0.0125(\pm 0.0014)_{stat}(\pm^{0.0002}_{0.0004})_{contamination}$	
$\epsilon^{t\bar{t}MC}_{VBF}$	$0.0170(\pm 0.0016)_{stat}$	

Table 5.4: Data and MC event yields for $t\bar{t}$ CR1 OS. Purity is based on MC while the scale factor is calculated as $\frac{Data - MC^{\neq t\bar{t}}}{MC^{t\bar{t}}}$.

LS		
Background	CR1 Expectation	CR1 Expectation ($m_{jj} > 250$)
$t\bar{t}$	597.0 $\pm_{stat}$ 20.0	10.7 $\pm_{stat}$ 2.7
$Z \to \tau\tau$	5.0 $\pm_{stat}$ 2.0	0 $+_{stat}$ 0.8
$Z \to \mu\mu$	1.1 $\pm_{stat}$ 1.1	0 $+_{stat}$ 1.1
$Z \to ee$	0 $+_{stat}$ 1.0	0 $+_{stat}$ 1.0
$W \to l\nu + 0jets$	0 $+_{stat}$ 41.2	0 $+_{stat}$ 41.2
$W \to l\nu + 1jets$	6.0 $\pm_{stat}$ 6.0	0 $+_{stat}$ 6.0
$W \to l\nu + 2jets$	23.9 $\pm_{stat}$ 6.4	0 $+_{stat}$ 1.7
$W \to l\nu + 3jets$	27.1 $\pm_{stat}$ 5.0	0.9 $\pm_{stat}$ 0.9
$W \to l\nu + 4jets$	41.0 $\pm_{stat}$ 7.3	0 $+_{stat}$ 1.3
WW	1.9 $\pm_{stat}$ 0.6	0 $+_{stat}$ 0.2
WZ	26.5 $\pm_{stat}$ 0.6	0.35 $\pm_{stat}$ 0.07
$ZZ \to ll\nu\nu$	0.06 $\pm_{stat}$ 0.04	0 $+_{stat}$ 0.03
$ZZ \to llll$	1.11 $\pm_{stat}$ 0.04	0.006 $\pm_{stat}$ 0.003
W^+W^+qq	5.0 $\pm_{stat}$ 0.5	0.2 $\pm_{stat}$ 0.1
W^-W^-qq	1.7 $\pm_{stat}$ 0.2	0.20 $\pm_{stat}$ 0.06
$H \to \tau\tau$	0.010 $\pm_{stat}$ 0.004	0.001 $\pm_{stat}$ 0.001
$H \to WW$	0.010 $\pm_{stat}$ 0.005	0.002 $\pm_{stat}$ 0.002
$H \to ZZ \to ll\nu\nu$	0.0002 $\pm_{stat}$ 0.0002	0 $+_{stat}$ 0.0001
$H \to ZZ \to llll$	0.010 $\pm_{stat}$ 0.003	0.002 $\pm_{stat}$ 0.001
Total MC	737.5 $\pm^{47.5}_{23.7}$	12.4 $\pm^{41.8}_{2.8}$
Purity	81.0%	86.2%
Data	877	16
SF	1.234 $(\pm^{0.067}_{0.097})_{stat}$ $(\pm^{0.045}_{0.043})_{lumi}$	1.333 $(\pm^{0.507}_{1.333})_{stat}$ $(\pm^{0.046}_{0.044})_{lumi}$
ϵ^{Data}_{VBF}	$0.0194(\pm 0.0051)_{stat}(\pm^{0.0009}_{0.0037})_{contamination}$	
$\epsilon^{t\bar{t}MC}_{VBF}$	$0.0180(\pm 0.0054)_{stat}$	

Table 5.5: Data and MC event yields for $t\bar{t}$ CR1 LS. Purity is based on MC while the scale factor is calculated as $\frac{Data - MC^{\neq t\bar{t}}}{MC^{t\bar{t}}}$.

OS	
Background	CR2 Expectation
$t\bar{t}$	1320.7 $\pm_{stat}$ 29.7
$Z \to \tau\tau$	303.3 $\pm_{stat}$ 16.2
$Z \to \mu\mu$	35.9 $\pm_{stat}$ 6.4
$Z \to ee$	1.0 $\pm_{stat}$ 1.0
$W \to l\nu + 0jets$	0 $+_{stat}$ 41.2
$W \to l\nu + 1jets$	17.9 $\pm_{stat}$ 10.3
$W \to l\nu + 2jets$	82.2 $\pm_{stat}$ 11.9
$W \to l\nu + 3jets$	88.5 $\pm_{stat}$ 8.9
$W \to l\nu + 4jets$	97.6 $\pm_{stat}$ 11.2
WW	254.2 $\pm_{stat}$ 6.7
WZ	68.4 $\pm_{stat}$ 0.9
$ZZ \to ll\nu\nu$	1.1 $\pm_{stat}$ 0.2
$ZZ \to llll$	2.01 $\pm_{stat}$ 0.06
W^+W^+qq	0.3 $\pm_{stat}$ 0.1
W^-W^-qq	0.07 $\pm_{stat}$ 0.04
$H \to \tau\tau$	1.13 $\pm_{stat}$ 0.04
$H \to WW$	4.2 $\pm_{stat}$ 0.1
$H \to ZZ \to ll\nu\nu$	0.0047 $\pm_{stat}$ 0.0007
$H \to ZZ \to llll$	0.014 $\pm_{stat}$ 0.003
Total MC	2278.5 $\pm^{58.2}_{41.1}$
Purity	58.0%
Data	2508
SF	1.120 $(\pm^{0.051}_{0.062})_{stat}$ $(\pm^{0.058}_{0.056})_{lumi}$

Table 5.6: Data and MC event yields for $t\bar{t}$ CR2 OS. Purity is based on MC while the scale factor is calculated as $\frac{Data - MC^{\neq t\bar{t}}}{MC^{t\bar{t}}}$.

LS	
Background	CR2 Expectation
$t\bar{t}$	206.8 $\pm_{stat}$ 12.9
$Z \to \tau\tau$	7.4 $\pm_{stat}$ 2.5
$Z \to \mu\mu$	4.4 $\pm_{stat}$ 2.2
$Z \to ee$	0 $+_{stat}$ 1.0
$W \to l\nu + 0jets$	0 $+_{stat}$ 41.3
$W \to l\nu + 1jets$	6.0 $\pm_{stat}$ 6.0
$W \to l\nu + 2jets$	53.0 $\pm_{stat}$ 9.5
$W \to l\nu + 3jets$	67.8 $\pm_{stat}$ 7.8
$W \to l\nu + 4jets$	55.2 $\pm_{stat}$ 8.4
WW	5.5 $\pm_{stat}$ 1.0
WZ	67.9 $\pm_{stat}$ 0.9
$ZZ \to ll\nu\nu$	0.06 $\pm_{stat}$ 0.04
$ZZ \to llll$	1.91 $\pm_{stat}$ 0.05
W^+W^+qq	9.8 $\pm_{stat}$ 0.7
W^-W^-qq	3.2 $\pm_{stat}$ 0.2
$H \to \tau\tau$	0.026 $\pm_{stat}$ 0.006
$H \to WW$	0.027 $\pm_{stat}$ 0.008
$H \to ZZ \to ll\nu\nu$	0.0007 $\pm_{stat}$ 0.0003
$H \to ZZ \to llll$	0.017 $\pm_{stat}$ 0.003
Total MC	489.0 $\pm^{46.3}_{20.9}$
$t\bar{t}$ Purity	42.3%
Data	586
SF	1.249 $(\pm^{0.170}_{0.280})_{stat}$ $(\pm^{0.088}_{0.082})_{lumi}$

Table 5.7: Data and MC event yields for $t\bar{t}$ CR2 LS. Purity is based on MC while the scale factor is calculated as $\frac{Data - MC^{\neq t\bar{t}}}{MC^{t\bar{t}}}$.

$t\bar{t}$	$N^{data}_{CR2} - N^{\neq t\bar{t}MC}_{CR2}$	ϵ^{Data}_{VBF}	$N^{t\bar{t}}_{Signal}$	$N^{t\bar{t}MC}_{Signal}$
OS	1516.4 $(\pm^{76.3}_{87.7})_{stat}$	$0.0125(\pm 0.0014)_{stat}(\pm^{0.0002}_{0.0004})_{contamination}$	19.0 $(\pm^{2.3}_{2.4})_{stat}$	22.8 $(\pm 3.9)_{stat}$
LS	282.4 $(\pm^{43.5}_{62.6})_{stat}$		3.5 $(\pm^{0.7}_{0.9})_{stat}$	2.0 $(\pm 1.2)_{stat}$

Table 5.8: $t\bar{t}$ estimation summary.

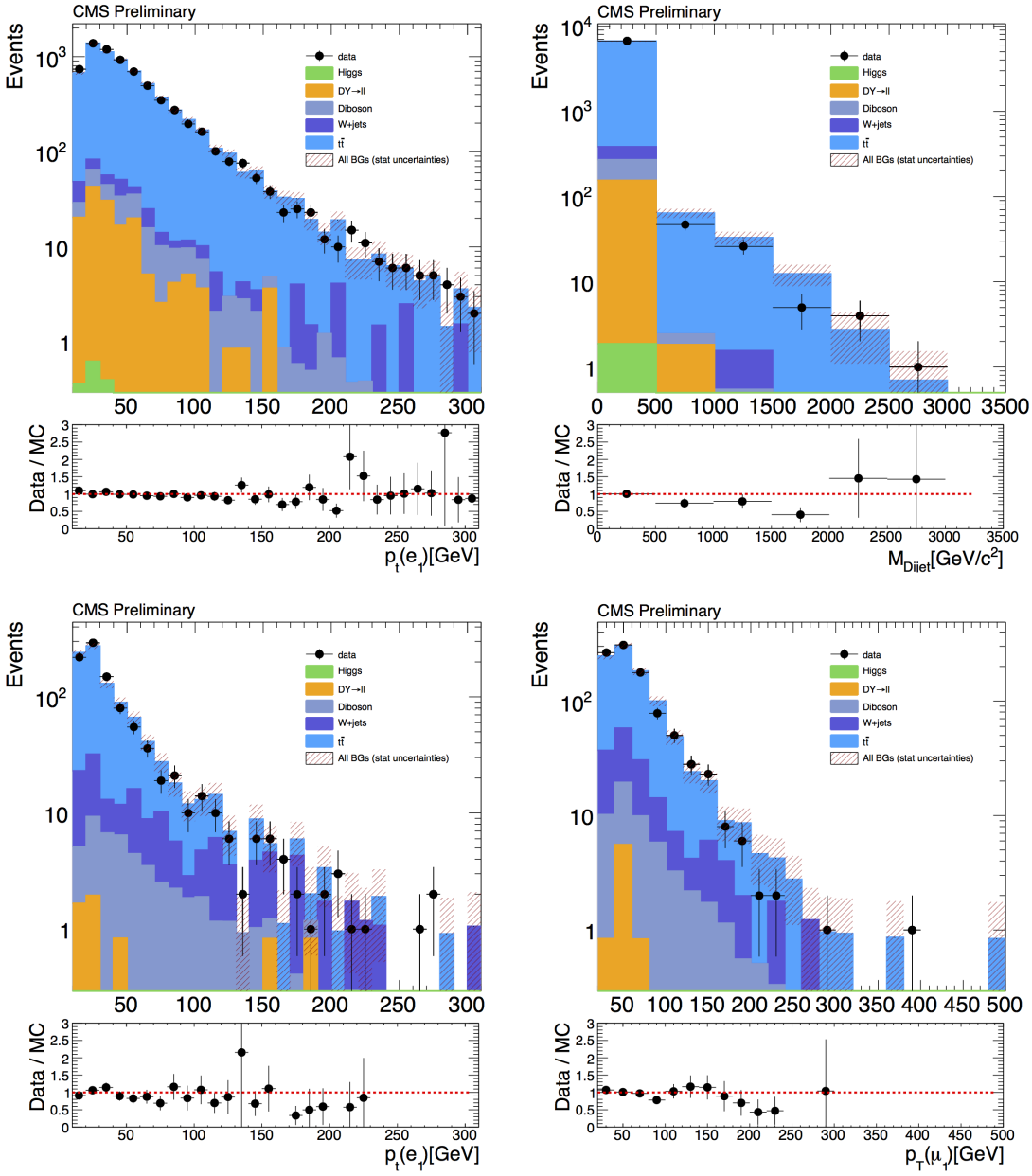

Figure 5.4: From left to right on the top row is e p_T and m_{jj} in OS CR1. The bottom row is e p_T and μ p_T in LS CR1

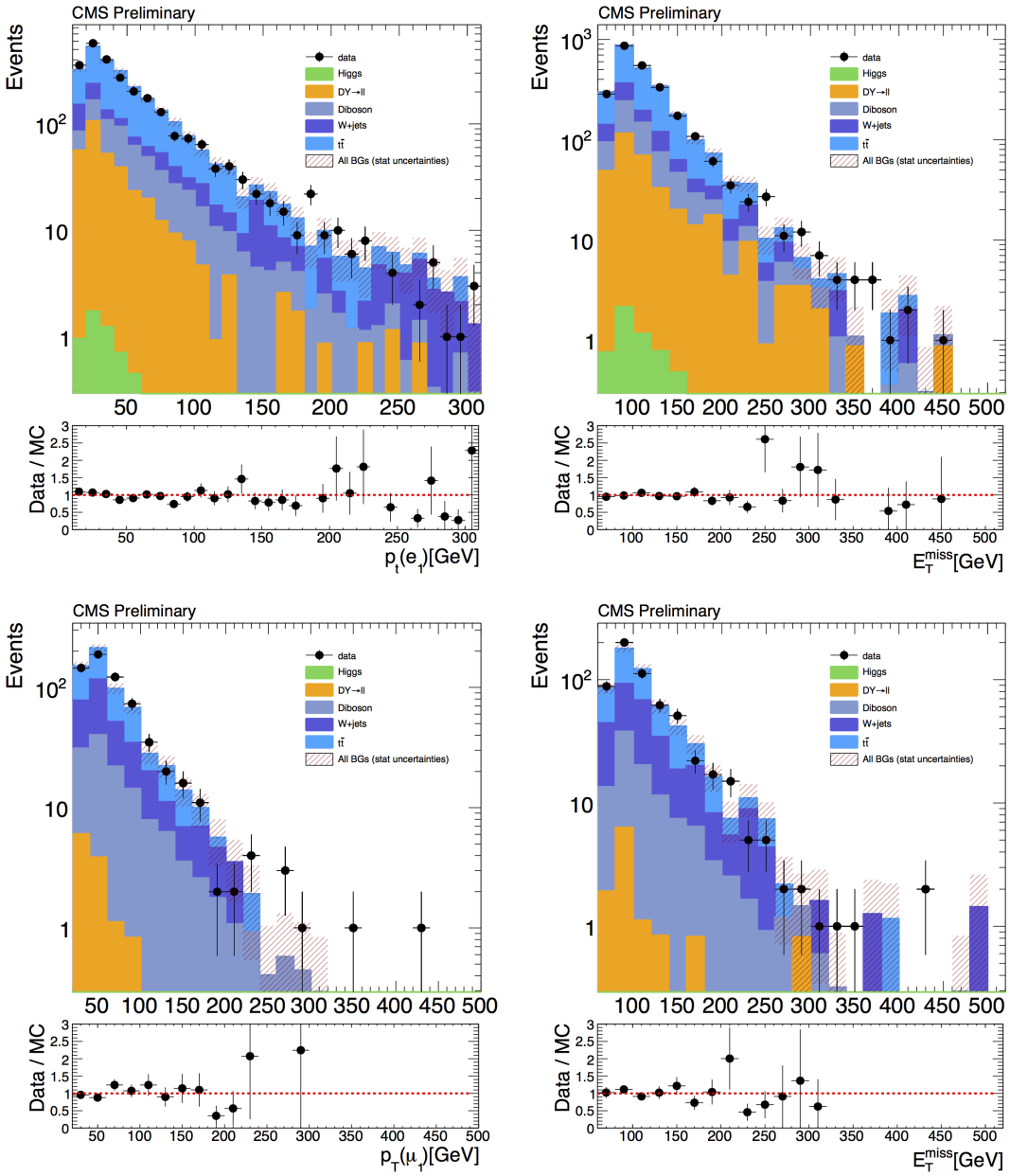

Figure 5.5: From left to right on the top row is e p_T and $\not\!\!E_{\rm T}$ in OS CR2. The bottom row is μ p_T and $\not\!\!E_{\rm T}$ in LS CR2.

us to correct the MC-based rate in our signal region.

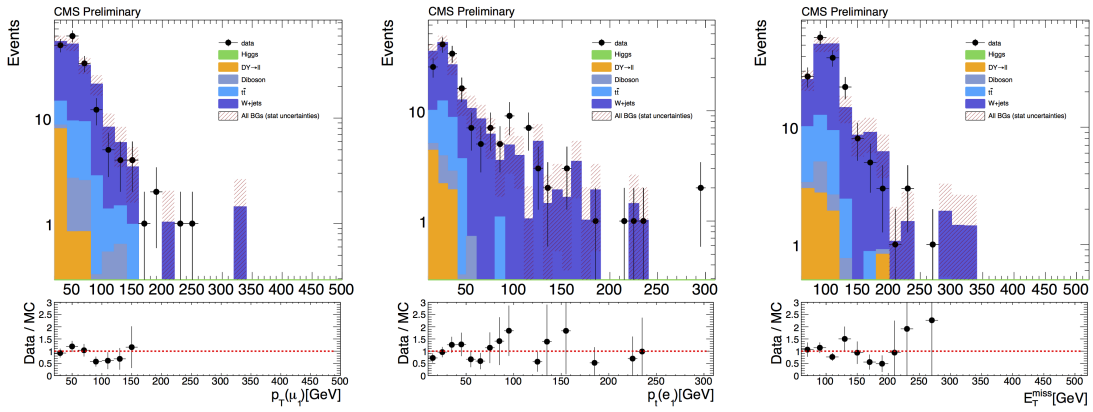

Figure 5.6: μ p_T, e p_T, and $\not{E}_{\mathrm{T}}$, in WCR from left to right.

5.3.3 Diboson Background Estimation

Diboson events compose only a small portion of our OS signal region as compared to the $t\bar{t}$ background. Though still dominant $t\bar{t}$ only sneaks into our LS signal region when one of the lepton charges is misdiagnosed. As a result, backgrounds with real LS lepton pairs become more important. In particular, $W^{\pm}W^{\pm} \rightarrow l^{\pm}l^{\pm}$, $W^{\pm}Z^{0} \rightarrow l^{\pm}l^{+}l^{-}\nu$, and $Z^{0}Z^{0} \rightarrow l^{\pm}l^{\mp}l^{\pm}l^{\mp}$, all provide real LS lepton pairs and compose almost half of our LS signal region. Since the diboson leptons are real, prompt leptons, they are well understood and modeled by MC. There is also real $\not{E}_{\mathrm{T}}$ from neutrinos and thus this portion of the event is similarly well-modeled. The largest uncertainty with diboson contamination to the signal region is the rate at which these backgrounds radiate jets which pass the VBF cuts. As a result, we form a data-driven diboson control region by removing the VBF jet requirements and require 3 prompt muons. The kinematics of this region can be seen in Figure 5.7.

Background	WCR Expectation
$W \to l\nu$ total	121.6 $(\pm^{43.5}_{12.6})_{stat}$
$W \to l\nu + 0jets$	0 $+_{stat}$ 41.2
$W \to l\nu + 1jets$	0 $+_{stat}$ 6.0
$W \to l\nu + 2jets$	42.8 $\pm_{stat}$ 8.6
$W \to l\nu + 3jets$	41.7 $\pm_{stat}$ 6.1
$W \to l\nu + 4jets$	37.2 $\pm_{stat}$ 6.9
$t\bar{t}$	18.8 $\pm_{stat}$ 3.5
$Z \to \tau\tau$	4.1 $\pm_{stat}$ 1.8
$Z \to \mu\mu$	4.3 $\pm_{stat}$ 2.2
$Z \to ee$	0 $+_{stat}$ 1.0
WW	3.2 $\pm_{stat}$ 0.7
WZ	1.2 $\pm_{stat}$ 0.1
$ZZ \to ll\nu\nu$	0.08 $\pm_{stat}$ 0.05
$ZZ \to llll$	0.052 $\pm_{stat}$ 0.009
W^+W^+qq	0.15 $\pm_{stat}$ 0.09
W^-W^-qq	0.05 $\pm_{stat}$ 0.03
$H \to \tau\tau$	0.019 $\pm_{stat}$ 0.005
$H \to WW$	0.012 $\pm_{stat}$ 0.005
$H \to ZZ \to ll\nu\nu$	0.0003 $\pm_{stat}$ 0.0002
$H \to ZZ \to llll$	0 $+_{stat}$ 0.0007
Total MC	153.6 $\pm^{43.7}_{13.4}$
Purity	79.2%
Data	168
SF	1.118 $(\pm^{0.162}_{0.415})_{stat}$ $(\pm^{0.043}_{0.040})_{lumi}$

Table 5.9: Data and MC event yields for $W \to l\nu$ + jets control region. Purity is based on MC while the scale factor is calculated as $\frac{Data - MC^{\neq W \to l\nu}}{MC^{W \to l\nu}}$.

Using this control region, we obtain a data-to-MC scale factor of 1.12±0.06.

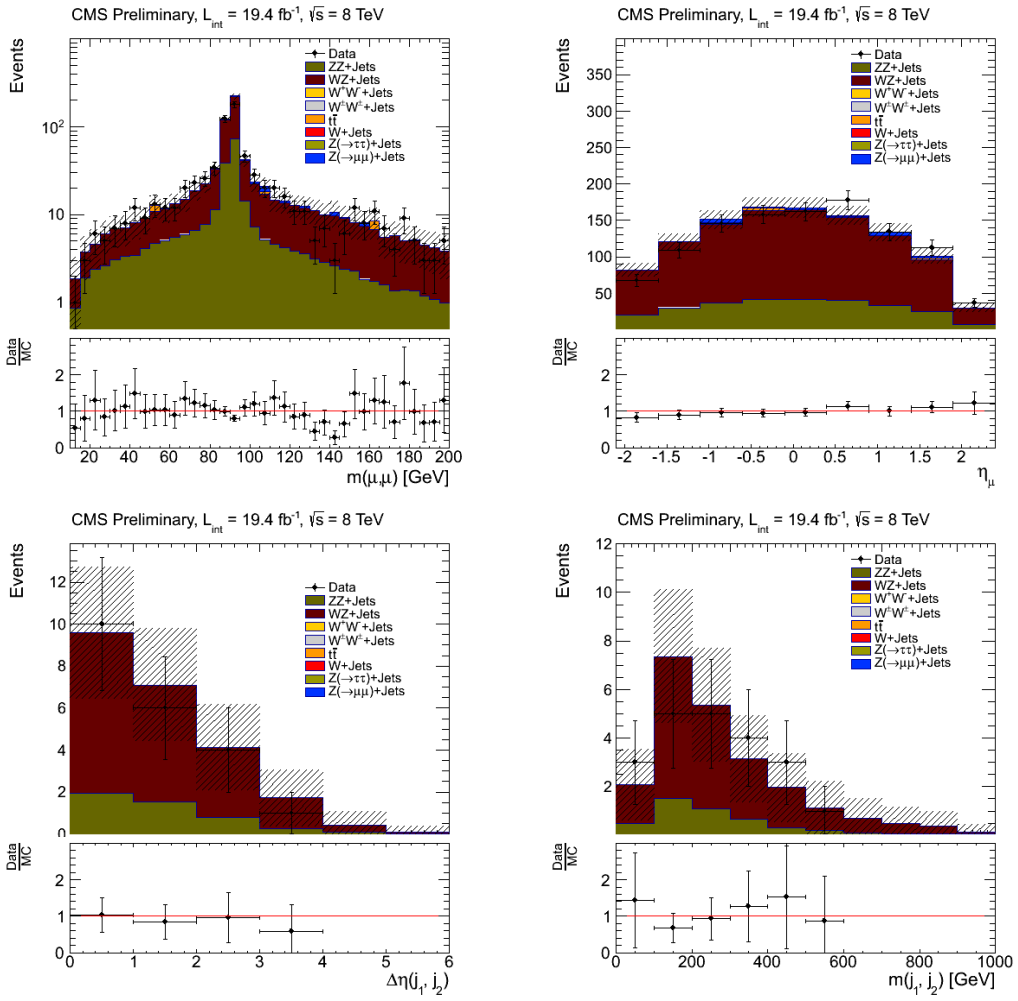

Figure 5.7: From left to right: $m_{\mu\mu}$, $\eta(\mu)$, $\Delta\eta(j,j)$, and m_{jj} distributions for the WZ/ZZ Diboson CR.

5.4 Closure Tests

Our $t\bar{t}$ estimation relies on the dijet cuts having the same efficiency in the case of 0 and 1 b-jets. This is a result of measuring the m_{jj} cut efficiency in a 1 b-jet control region and applying this to a 0 b-jet control region in order to extrapolate

to the signal region. Along similar lines, since the m_{jj} efficiency is taken from the OS control regions and applied to the LS estimation, it is similarly important that different lepton sign combinations have the same m_{jj} shape. As a closure test, the normalized m_{jj} spectrum is over-plotted for these two cases in Figure 5.8.

Also, as was mentioned in section 5.3.1, another closure test was performed by comparing the prediction to signal region yield with only simulation. The difference in these closure tests is prescribed as a systematic uncertainty. In this case it is 1.2%. In the case of Figure 5.8, the ratio plot is fit to a constant and the uncertainty is taken as the closure systematic.

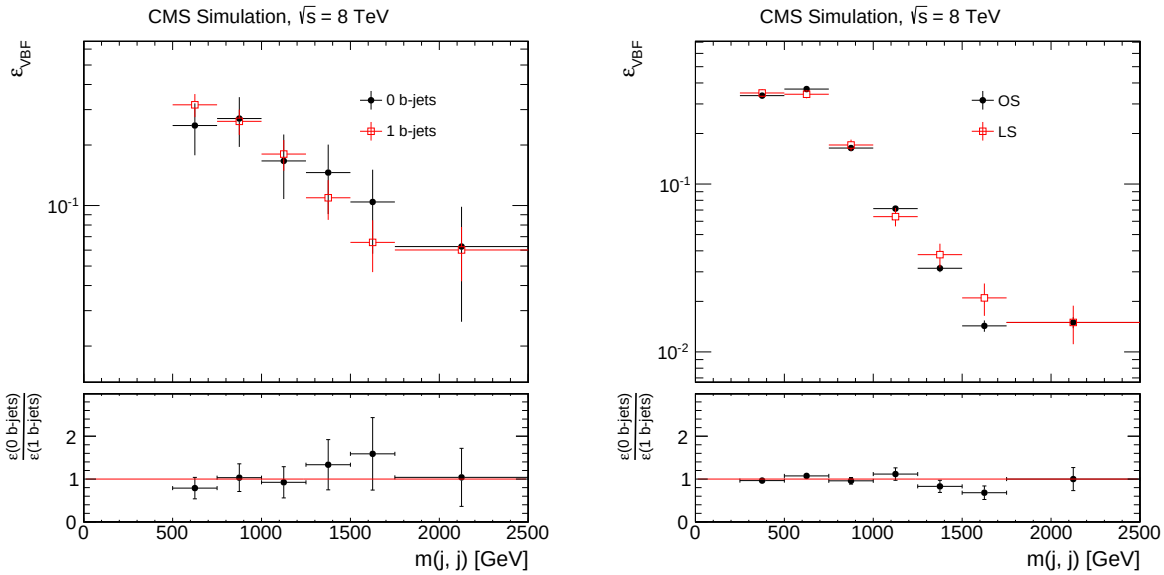

Figure 5.8: The m_{jj} spectrum comparison between the 0 and 1 b-jets (left) and OS and LS $e\mu$ pairs (right).

5.5 Systematic Uncertainties

a systematic uncertainty is prescribed for the possible bias to our measured VBF cut efficiency resulting from impurities in CR1. The systematic uncertainties on the non-$t\bar{t}$ backgrounds are determined by considering and propagating the uncertainties from ISR/FSR, luminosity (2.6%), μ trigger (2%), μ ID (1%), electron ID (2% for EB, 4% for EE), and b-tagging ID (4%, 25% for fakes). The uncertainties on the non-$t\bar{t}$ backgrounds are then propagated when performing the subtraction from data in Equation 5.1. This results in a systematic uncertainty of approximately 3.2% due to contamination. A summary of these uncertainties for each background are given in Table 5.10

Source	Uncertainty	Signal	$t\bar{t}$	V+jets	VV
PDF	—	6%	3.5%	3.5%	3.5%
ISR/FSR	—	2%	2%	2%	2%
Luminosity	2.6%	2.6%	2.6%	2.6%	2.6%
Muon Trig	2%	2%	2%	2%	2%
Muon ID	1%	1%	1%	1%	1%
Electron ID	2% (4%)	3%	3%	3%	3%
b-Jet ID	4% (25%)	1%	5%	1%	1%
Contamination	—	—	3.2%	—	—
Closure	—	—	2%	20%	1%

Table 5.10: Summary of systematic uncertainties over all backgrounds. The two values for electron ID indicate the uncertainties in the barrel and endcap regions, respectively. The two values for b-Jet ID indicate the uncertainty for b-jet efficiency and misidentification, respectively.

5.6 Signal Benchmark Points

As discussed previously, our signal region is sensitive to potential $\widetilde{\chi^0}$, $\widetilde{\chi^{\pm}}$, $\widetilde{l^{\pm}}$, and $\widetilde{\nu}$ particles with various combinations of decay patterns. The natural question arises

as to what sort of benchmark our search should assume. We take a simplified point of $\widetilde{\chi_2^0} - \widetilde{\chi_1^\pm}$ production where the neutralino decays as $\widetilde{\chi_2^0} \to \widetilde{l^\pm} l^\mp \to l^\pm l^\mp \widetilde{\chi_1^0}$ and the chargino decays as $\widetilde{\chi^\pm} \to l^\pm \nu_l \widetilde{\chi_1^0}$ (see Figure 5.1). We take the $\widetilde{\chi_1^0}$ to be massless, $m_{\widetilde{\chi_1^\pm}} - m_{\widetilde{l^\pm}} = m_{\widetilde{\chi_2^0}} - m_{\widetilde{l^\pm}} = 5$ GeV, and $m_{\widetilde{\chi_1^\pm}} = m_{\widetilde{\chi_2^0}}$. $m_{\widetilde{\chi_1^\pm}} = m_{\widetilde{\chi_2^0}}$ is a reasonable assumption in cases where $\widetilde{\chi_1^0}$ is largely Bino and $\widetilde{\chi_2^0}$ and $\widetilde{\chi_1^\pm}$ are largely Wino. The $l^\pm$ represents both $\mu^\pm$ and $e^\pm$. In particular, this mass hierarchy assumes that $\widetilde{e^\pm}$ and $\widetilde{\mu^\pm}$ are 5 GeV lighter than our gauginos, while $\widetilde{\tau^\pm}$ is heavier. The neutralino emits one hard and one soft lepton, while the chargino emits one hard lepton. Since our simplified scenario has only one free parameter, limits are set as a function of $m_{\widetilde{\chi_1^\pm}} = m_{\widetilde{\chi_2^0}}$. The cross section, total acceptance, and event yields for four of our points is in Table 5.11.

As with background samples, Madgraph 5 was used for parton level simulation while Pythia 6 dictated the subsequent hadronization [55][56]. The mass spectrum was created using ISAJET [60] using SUSY Les Houches accord [61] to interface with Madgraph.

$m_{\widetilde{\chi_1^\pm}} = m_{\widetilde{\chi_2^0}}$	Cross Section [fb]	Signal Acceptance (%)	Event Yield
$m_{\widetilde{\chi}} = 100$	47.9	8.4	39.8
$m_{\widetilde{\chi}} = 200$	11.7	11.2	12.9
$m_{\widetilde{\chi}} = 300$	4.4	12.4	5.3
$m_{\widetilde{\chi}} = 400$	1.0	12.9	1.3

Table 5.11: Cross section, acceptance, and expected signal region yield for 4 of our benchmark points.

5.7 Bayesian Limit Setting

95% confidence level (CL) upper limits on cross sections are derived by considering the event likelihoods across all channels:

$$\mathcal{L}(\bar{n}|\sigma,\bar{b},\bar{\epsilon}) = \prod_{i=1}^{N} \frac{\mu_i^{n_i} e^{-\mu_i}}{n_i!} \tag{5.2}$$

where μ_i is the expected number of events given a luminosity (L_i), signal efficiency (ϵ_i), and background expectation (b_i).

Given a probability density, we can derive a 95% upper limit on the cross section (σ_{95}):

$$\int_0^{\sigma_{95}} = \mathcal{P}(\sigma'|\bar{n},\bar{b},\bar{\epsilon})d\sigma' = 0.95 \tag{5.3}$$

Monte Carlo integration allows offsets in μ_i to be considered for both correlated and uncorrelated systematic uncertainties. See [63][64] for nice discussions with concrete examples. Within CMS, the probability density is given by the log-likelihood ratio of a signal and background H_1 versus only background H_0 hypothesis.

$$LLR = -2ln\frac{p(data|H_1)}{p(data|H_0)} \tag{5.4}$$

See [65] for a more complete discussion of the CL_s technique.

5.8 Results

A summary of all our control regions is given in Table 5.12. A summary of the background prediction of each sample is given in Table 5.13 and Table 5.14 for OS and LS, respectively. A summary of the final background prediction and data observation are given in Table 5.15. No excess is observed over the SM. As mentioned

previously, a soft m_{jj} cut of 250 is used for the signal region values stated here. This soft cut allows us to apply a shape based analysis, combining Bayesian limits from each bin of the m_{jj} spectrum. This technique allows both for reasonable statistics, as can be seen in Table 5.15, but allows data points with larger m_{jj} to be given a larger weight in the final limit setting. Using a simple 'cut and count' analysis would having a loose signal region with reasonable statistics but a lower $\frac{S}{\sqrt{S+B}}$, or a tighter signal region with poor statistics but a higher $\frac{S}{\sqrt{S+B}}$. This shape based Bayesian fitting technique not only combines the OS and LS channels, but also combines the information of each m_{jj} bin individually, allowing for maximum sensitivity.

The m_{jj} spectrum of our signal region can be seen in Figure 5.9. The subsequent 95% CL upper limits can be seen in Figure 5.10. Only statistical errors are shown in Figure 5.9 while the final fitting in Figure 5.10 includes both statistical and systematic uncertainties. Gaugino masses ($m_{\widetilde{\chi_1^\pm}} = m_{\widetilde{\chi_2^0}}$) are excluded to 350 GeV.

Sample	$t\bar{t}$ OS CR1	$t\bar{t}$ OS CR2	$t\bar{t}$ LS CR1	$t\bar{t}$ LS CR2	$W \to l\nu$ CR
W^+W^-	76.3 ± 3.7	254.2 ± 6.7	1.9 ± 0.6	5.5 ± 1.0	3.2 ± 0.7
$W^\pm W^\pm$	0.3 ± 0.1	0.4 ± 0.1	6.7 ± 0.5	13.0 ± 0.7	0.2 ± 0.1
WZ	26.0 ± 0.6	68.4 ± 0.9	26.5 ± 0.6	67.9 ± 0.9	1.2 ± 0.1
ZZ	1.2 ± 0.1	3.1 ± 0.2	1.2 ± 0.1	2.0 ± 0.1	0.13 ± 0.05
$W + Jets$	$102.3 \pm^{12.7}_{11.2}$	286.2 ± 21.3	98.1 ± 12.4	181.9 ± 16.1	$121.6 \pm^{13.9}_{12.6}$
$t\bar{t}$	6317.2 ± 65.4	1320.7 ± 29.7	597.0 ± 20.0	206.8 ± 12.9	18.8 ± 3.5
$Z \to \tau\tau$	141.3 ± 10.9	303.3 ± 16.2	5.0 ± 2.0	7.4 ± 2.5	4.1 ± 1.8
$Z \to \mu\mu$	13.8 ± 4.0	35.9 ± 6.4	1.2 ± 1.2	4.4 ± 2.2	4.3 ± 2.2
$Z \to ee$	$0 \pm^{1.0}_{0.0}$	1.0 ± 1.0	$0 \pm^{1.0}_{0.0}$	$0 \pm^{1.0}_{0.0}$	$0 \pm^{1.0}_{0.0}$
Higgs	2.0 ± 0.1	5.3 ± 0.1	0.07 ± 0.01	0.07 ± 0.01	0.03 ± 0.01
Total MC	$6680.9 \pm^{67.7}_{67.5}$	2312.3 ± 42.5	737.5 ± 23.7	510.4 ± 22.4	$153.6 \pm^{14.7}_{13.4}$
Purity	94.6%	57.1%	81.0%	40.5%	79.2%
Data	6775	2508	877	586	168
Scale Factor	1.01 ± 0.02	1.12 ± 0.05	1.23 ± 0.07	1.25 ± 0.17	$1.12 \pm^{0.16}_{0.17}$

Table 5.12: Summary table of all control regions for the $e\mu$ final state.

OS					
Sample	N^{MC}_{central}	SF^{CR}_{central}	ϵ^{MC}_{VBF}	ϵ^{data}_{VBF} (or SF^{CR}_{VBF})	N_{signal}
Diboson	8.2×10^2	1.12 ± 0.06	0.0034 ± 0.0020	—	3.1 ± 0.7
$t\bar{t}$	1.8×10^3	—	0.0170 ± 0.0016	0.0125 ± 0.0014	$19.0 \pm^{2.3}_{2.4}$
$W \to l\nu$	3.4×10^3	$1.12 \pm^{0.16}_{0.17}$	0.0011 ± 0.0006	—	$4.2 \pm^{3.3}_{2.5}$
DY	4.1×10^2	—	0.0104 ± 0.0054	—	$3.7 \pm^{2.1}_{1.9}$
Higgs	5.6×10^0	—	0.1936 ± 0.1670	—	1.1 ± 0.5
BG Prediction	—	—	—	—	$31.1 \pm^{4.6}_{4.0}$
Signal	—	—	—	—	22
Data	—	—	—	—	39.8

Table 5.13: Background estimation summary for the OS $e\mu$ final state.

LS					
Sample	N^{MC}_{central}	SF^{CR}_{central}	ϵ^{MC}_{VBF}	ϵ^{data}_{VBF} (or SF^{CR}_{VBF})	N_{signal}
Diboson	1.4×10^2	1.12 ± 0.06	0.0017 ± 0.0017	—	$1.9 \pm^{0.4}_{0.2}$
$t\bar{t}$	2.7×10^2	—	0.0180 ± 0.0054	0.0125 ± 0.0014	$3.5 \pm^{0.7}_{0.9}$
$W \to l\nu$	4.2×10^2	$1.12 \pm^{0.16}_{0.17}$	$0 \pm^{0.0024}_{0}$	—	$0 \pm^{3.0}_{0}$
DY	3.6×10^1	—	$0 \pm^{0.27}_{0}$	—	$0 \pm^{1.7}_{0}$
Higgs	< 0.1	—	—	—	—
BG Prediction	—	—	—	—	$5.4 \pm^{3.5}_{0.9}$
Signal	—	—	—	—	5
Data	—	—	—	—	39.8

Table 5.14: Background estimation summary for the LS $e\mu$ final state.

	OS		LS	
	Final Prediction	MC Prediction	Final Prediction	MC Prediction
$t\bar{t}$	19.0 $(\pm^{2.3}_{2.4})_{stat}$	22.8 $(\pm 3.9)_{stat}$	3.5 $(\pm^{0.7}_{0.9})_{stat}$	2.0 $(\pm 1.2)_{stat}$
DY	3.7 $(\pm^{2.1}_{1.9})_{stat}$	3.7 $(\pm^{2.1}_{1.9})_{stat}$	0 $(+1.7)_{stat}$	0 $(+1.7)_{stat}$
$W \to l\nu$	4.2 $(\pm^{3.3}_{2.5})_{stat}$	3.8 $(\pm^{2.9}_{2.2})_{stat}$	0 $(+3.0)_{stat}$	0 $(+2.7)_{stat}$
Diboson	3.1 $(\pm 0.7)_{stat}$	2.8 $(\pm 0.6)_{stat}$	1.9 $(\pm^{0.4}_{0.2})_{stat}$	1.7 $(\pm^{0.3}_{0.2})_{stat}$
Higgs	1.1 $(\pm 0.5)_{stat}$	1.1 $(\pm 0.5)_{stat}$		<0.01
Total	31.1 $(\pm^{4.6}_{4.0})_{stat}$	34.2 $(\pm^{5.4}_{4.9})_{stat}$	5.4 $(\pm^{3.5}_{0.9})_{stat}$	3.7 $(\pm^{3.4}_{1.2})_{stat}$
Data	$22(\pm 4.7)_{stat}$		$5(\pm 2.2)_{stat}$	
$m_{\tilde{\chi}} = 100$	39.8			
$m_{\tilde{\chi}} = 200$	12.9			
$m_{\tilde{\chi}} = 300$	5.3			
$m_{\tilde{\chi}} = 400$	1.3			

Table 5.15: Background prediction summary for both opposite and like-sign as well as the number of data events observed. The bottom rows denote the number of predicted events in our benchmark points for a given gaugino mass in GeV. The numbers are equal for LS and OS since our benchmark point has equal probability for the two cases.

As a basis for comparison, limits in a similar CMS analysis with the same luminosity are given in Figure 5.11 [62]. We find similar sensitivity to the other CMS dilepton search even before adding the $\mu\mu$ and ee channels.

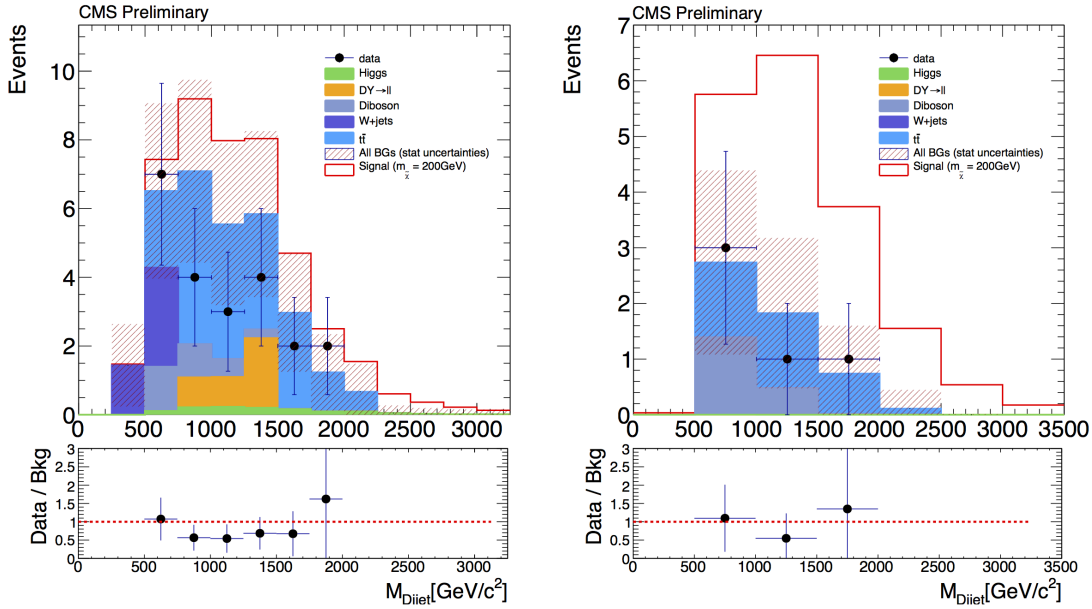

Figure 5.9: The $e\mu$ signal region as a function of m_{jj} for OS (left) and LS (right).

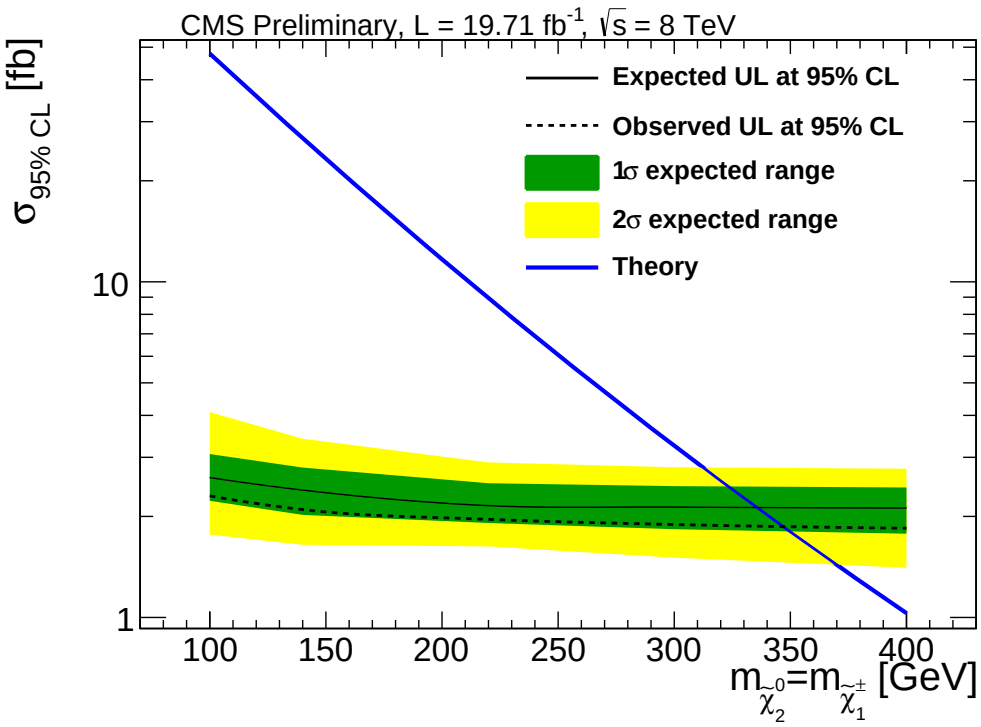

Figure 5.10: Expected (solid black) and observed (dashed black) 95% CL cross section upper limits as a function of $m_{\widetilde{\chi}_1^{\pm}} = m_{\widetilde{\chi}_2^0}$. The green and yellow bands dictate the one and two standard deviation variations in the expected limits. The blue line is the theoretical cross sections of our benchmark scenario.

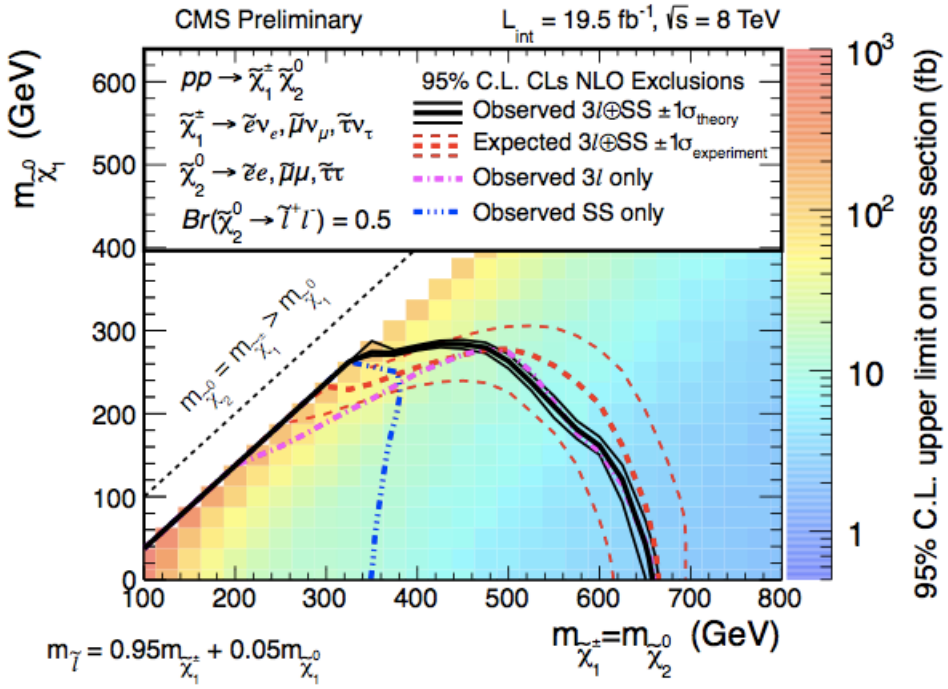

Figure 5.11: Limits from another CMS analysis [62] using the full 2012 8TeV dataset. Their signal topology is roughly equivalent to the benchmark point used in in this search where $m_{\tilde{\chi}_1^0} = 0$.

6. CONCLUSION

This search reveals no sign of physics beyond the Standard Model. In certain regions of SUSY parameter space, sensitivity can be gained by triggering off of the WBF jets rather than the prompt leptons. The main benefit of this is that lepton p_T thresholds could be reduced since there is no longer leptonic trigger bias. Furthermore, searches can be done for '0 lepton' final states, which could reveal WBF dark matter production ($\widetilde{\chi}_1^0\widetilde{\chi}_1^0$) or compressed SUSY scenarios where leptons are far too soft to be observed in our detector. On the other hand, these triggers require stringent WBF jet cuts, possibly depleting a small signal.

Both SUSY and WBF processes remain particularly well motivated topics for the upcoming 14 TeV LHC data. If no colored SUSY particles are quickly found, then EWKino searches will once again come to the forefront. Similarly, WBF cross sections will decrease less than direct production as the LHC increases energy. This will make WBF processes an even better handle for new physics in uncharted territory.

All that is certain is that the next round of LHC data will present us with more questions than answers.

REFERENCES

[1] S. L. Glashow, Partial-Symmetries of Weak Interactions. *Nuclear Physics* 22, 579-588 (1961).

[2] S. Weinberg, A Model of Leptons. *Physical Review Letters* 19, 1264-1266 (1967).

[3] A. Salam, Elementary Particle Theory, Relativistic Groups and Analyticity. *Proceedings of the 8th Nobel Symposium*, 367-377. Almqvist & Wiksell, Stockholm (1968).

[4] M. Gell-Mann, Symmetries of Baryons and Mesons. *Physical Review* 125:3 1067-1084 (1962).

[5] PLUTO Collaboration, Jet Analysis of the Y(9.46) Decay into Charged Hadrons. *Physics Letters B* 82:3 449-462 (1979).

[6] Particle Data Group, 2012 Review of Particle Physics - Gauge and Higgs Bosons. *Physical Review D* 86:010001 (2012).

[7] CDF Collaboration, Observation of Top Quark Production in pp Collisions with the Collider Detector at Fermilab. *Physical Review Letters* 74:14 2626-2631 (1995).

[8] DO Collaboration, Search for High Mass Top Quark Production in pp Collisions at $\sqrt{s} = 1.8$ TeV. *Physical Review Letters* 74:14 2422-2426 (1995).

[9] DONUT Collaboration, Observation of Tau Neutrino Interactions. *Physics Letters B* 504:3 218-224 (2001).

[10] CMS Collaboration, Observation of a New Boson at a Mass of 125 GeV with the CMS Experiment at the LHC. *Physics Letters B* 716:1 30-61 (2012).

[11] ATLAS Collaboration, Observation of a New Particle in the Search for the Standard Model Higgs Boson with the ATLAS Detector at the LHC. *Physics Letters B* 716:1 1-29 (2012).

[12] R. Barbieri, G. Giudice, Upper Bounds on Supersymmetric Particle Masses. *Nuclear Physics B* 306:1 63-76 (1988).

[13] Muon g-2 Collaboration, Final Report of the E821 Muon Anomalous Magnetic Moment Measurement at BNL. *Physical Review D* 73:072003 (2006).

[14] P. Gambino, U. Haisch, M. Misiak, Determining the Sign of the b $\to$ sγ Amplitude. *Physical Review Letters* 94:061803 (2005).

[15] BaBar Collaboration, Exclusive Measurements of b $\to$ sγ Transition Rate and Photon Energy Spectrum. *Physical Review D* 86:052012 (2012).

[16] BaBar Collaboration, Evidence for an Excess of $\bar{B} \to D^{(*)}\tau^{-}\nu_{\tau}$ Decays. *Physical Review Letters* 109:101802 (2012).

[17] WMAP Collaboration Nine-Year Wilkinson Microwave Anisotropy Probe (WMAP) Observations: Final Maps and Results. *Astrophysical Journal Supplemental* 208:20 (2013).

[18] Planck Collaboration, Planck 2013 Results. XVI. Cosmological Parameters. *arXiv* 1303.5076 (2013).

[19] S. Dimopoulos, S. Raby, and F. Wilczek, Supersymmetry and the Scale of Unification. *Physical Review D* 24:6 1681-1683 (1981).

[20] S. Martin, A Supersymmetry Primer. *arXiv* hep-ph 9709356 (2011).

[21] A. Delannoy, B. Dutta, A. Gurrola, W. Johns, T. Kamon, et al., Probing Dark Matter at the LHC Using Vector Boson Fusion Processes. *Physical Review Letters* 111:061801 (2013).

[22] CMS Collaboration, Search for New Physics in the Multijet and Missing Transverse Momentum Final State in Proton-Proton Collisions at $\sqrt{s} = 7$ TeV. *Physical Review Letters* 109:171803 (2012).

[23] ATLAS Collaboration, Hunt for New Phenomena Using Large Jet Multiplicities and Missing Transverse Momentum with ATLAS in 4.7 fb^{-1} of $\sqrt{s} = 7$ TeV Proton-Proton Collisions. *Journal of High Energy Physics* 1207:167 (2012).

[24] CMS Collaboration, Search for Supersymmetry in All-Hadronic Events with Tau Leptons. *European Physical Journal C* 73:2493 (2013).

[25] B. Allanach and C. Lester, Multi-Dimensional mSUGRA Likelihood Maps. *Physical Review D* 73:015013 (2007).

[26] M. Citron, J. Ellis, F. Luo, J. Marrouche, K. A. Olive, K. J. de Vries, The End of the CMSSM Coannihilation Strip Is Nigh. *Physical Review D* 87:036012 (2012).

[27] B. Dutta, Flanagan W., Gurrola A., Johns W., Kamon T., et al., Probing Compressed Top Squarks at the LHC at 14 TeV. *Submitted to PRL* arxiv:1312.1348 (2013).

[28] CERN, LHC Design Report. *CERN-2004-003-V-1* (2004).

[29] D. Froidevaux and P. Sphicas, General-Purpose Detectors for the Large Hadron Collider. *Annual Review of Nuclear and Particle Science*, 56:375 (2006).

[30] ATLAS Collaboration, ATLAS Detector Physics and Performance : Technical Design Report Volume, 1. *CERN-LHCC-1999-014*, (1999).

[31] CMS Collaboration, CMS Physics : Technical Design Report Volume 1: Detector Performance and Software. *CERN-LHCC-2006-001*, (2006).

[32] CMS Collaboration, Precise Mapping of the Magnetic Field in the CMS Barrel Yoke using Cosmic Rays. *Journal of Instrumentation*, 5:T03021 (2010).

[33] CMS Collaboration, CMS Physics TDR: Volume II (PTDR2), Physics Performance. *CERN-LHCC-2006-021*, (2006).

[34] CMS Collaboration, CMS Upgrade TDR. *CERN-LHCC-2011-006*, (2011).

[35] D. Abbaneo, M. Abbresciab, M. Abi Aklc, C. Argamaingauda, P. Aspell, et al., Status of the Triple-GEM Project for the Upgrade of the CMS Muon System. *Journal of Instrumentation*, 8:C12031 (2013).

[36] D. Abbaneo, M. Abbresciab, M. Abi Aklc, C. Argamaingauda, P. Aspell, et al., Development and Performance of Large Scale Triple GEM for CMS. *Journal of Instrumentation*, 8:C11017 (2013).

[37] CMS Collaboration, Single Muon Efficiencies in 2012 Data. *CMS DP* 2013/009, (2013).

[38] CMS Collaboration, Particle-Flow Event Reconstruction in CMS and Performance for Jets, Taus and MET. *CMS PAS* PFT-09-001 (2009).

[39] CMS Collaboration, Performance of the Missing Transverse Energy Reconstruction in the 8 TeV Data. *CMS PAS* JME-12-002 (2012).

[40] G. Salam. Towards Jetography. *arXiv* 0906:1833v2 (2010).

[41] M. Cacciari, G. P. Salam, G. Soyez, The Anti-kt Jet Clustering Algorithm. *Journal of High Energy Physics* 0804:063 (2008).

[42] W. Adam, R. Fruhwirth, A. Strandlie, T. Todorov, Reconstruction of Electrons with the Gaussian-Sum Filter in the CMS Tracker at the LHC. *CMS Note* 2005-001 (2005).

[43] S. Baffioni, C. Charlot, F. Ferri, D. Futyan, P. Meridian, et al., Electron Reconstruction in CMS. *The European Physical Journal C* 49, 1099-1116 (2007).

[44] CMS Collaboration, Tau Reconstruction and Identification with Particle-Flow Techniques using the CMS Detector at LHC. *Nuclear Physics B - Proceedings Supplements* 189, 311-316 (2009).

[45] CMS Collaboration, Identification of b-quark Jets with the CMS Experiment. *Journal of Instrumentation* 8:P04013 (2013).

[46] S. Cahn, J. D. Dawson., Production of Very Massive Higgs Bosons. *Physics Letters B* 138, 196-200 (1984).

[47] Y. Dokshitzer, V. Khoze, S. Troyan, Physics in Collision VI. *Proceedings of the International Conference* p.365 World Scientific, Singapore (1987).

[48] J. Bjorken, Rapidity Gaps and Jets as a New-Physics Signature in Very-High-Energy Hadron-Hadron Collisions. *Physical Review D* 47:1 101-113 (1993).

[49] B. Mukhopadhyaya, A. Datta, P. Konar, Signals of Neutralinos and Charginos from Gauge Boson Fusion at the CERN Large Hadron Collider. *Physical Review D* 65:055008 (2002).

[50] G. C. Cho, K. Hagiwara, J. Kanzaki, T. Plehn, D. Rainwater, T. Stelzer, Weak Boson Fusion Production of Supersymmetric Particles at the LHC. *Physical Review D* 73:054002 (2006).

[51] G. Giudice, T. Han, K. Wang, L.T. Wang, Nearly Degenerate Gauginos and Dark Matter at the LHC. *Physical Review D* 81:115011 (2010).

[52] B. Dutta, A. Gurrola, W. Johns, T. Kamon, P. Sheldon, et al., Vector Boson Fusion Processes as a Probe of Supersymmetric Electroweak Sectors at the LHC. *Physical Review D* 87:035029 (2013).

[53] CMS Collaboration, *CMS* SUS-12-025 (under internal review), Search for Charginos and Neutralinos Produced in Vector Boson Fusion Processes in pp Collisions at $\sqrt{s} = 8$ TeV. (2012).

[54] R. Vogt, *Ultrarelativistic Heavy-Ion Collisions*. Elsevier, Oxford, UK (2007).

[55] J. Alwall, M. Herquet, F. Maltoni, O. Mattelaer, T. Stelzer, MadGraph 5: Going Beyond. *Journal of High Energy Physics* 1106:128 (2011).

[56] T. Sjostrand, S. Mrenna, P. Skands, Pythia 6.4 Physics and Manual. *Journal of High Energy Physics* 0605:026 (2006).

[57] J. Allison, K. Amako, J. Apostolakis, H. Araujo, P.A. Dubois, et al., Geant4 Developments and Applications. *Nuclear Science* 53:1 (2006).

[58] Z. Was, TAUOLA the Library for Tau Lepton Decay, and KKMC/KORALB/KORALZ/... Status Report. *arXiv* hep-ph/0011305 (2000).

[59] P. Nadolsky, H. L. Lai, Q. H. Cao, J. Huston, J. Pumplin, D. Stump, W. K. Tung, C. P. Yuan Implications of CTEQ Global Analysis for Collider Observables. *Physical Review D* 78:013004 (2008).

[60] P. Skands, B.C. Allanach, H. Baer, C. Balazs, G. Belanger, et al., SUSY Les Houches Accord: Interfacing SUSY Spectrum Calculators, Decay Packages, and Event Generators. *Journal of High Energy Physics* 07:036 (2004).

[61] H. Baer, F. Paige, S. Protopopescu, X. Tata, Simulating Supersymmetry with ISAJET 7.0 / ISASUSY 1.0. *arXiv* hep-ph 9005342 (1993).

[62] CMS Collaboration, Search for Electroweak Production of Charginos and Neutralinos using Leptonic Final States. *Submitted to EPJC* CMS-SUS-13-006 (2013).

[63] J. Conway, Setting Limits and Making Discoveries in CDF. *CDF Publication* 5236 (2000).

[64] J. Conway, Calculation of Cross Section Upper Limits Combining Channels Incorporating Correlated and Uncorrelated Systematic Uncertainties. *CDF Publication* 6428 (2005).

[65] A. Read, Presentation of Search Results: The CL(s) Technique. *Journal of Physics G: Nuclear and Particle Physics* 28:10 2693-2704(2002).

APPENDIX A

WEAK BOSON FUSION KINEMATICS

Pseudorapidity, η, is related to rapidity, y, and the azimuthal angle, θ, by:

$$\eta = -\ln\tan\frac{\theta}{2} \cong \frac{1}{2}\ln\frac{E+p_z}{E-p_z} = y \tag{A.1}$$

Taking the difference in pseaudorapidity for two particles:

$$\Delta\eta = \frac{1}{2}\ln\frac{E_1+p_{z1}}{E_1-p_{z1}} - \frac{1}{2}\ln\frac{E_2+p_{z2}}{E_2-p_{z2}} = \frac{1}{2}\ln\frac{E_1+p_{z1}}{E-p_{z1}}\frac{E_2-p_{z2}}{E_2+p_{z2}} \tag{A.2}$$

implies:

$$2\cosh\Delta\eta = \sqrt{\frac{E_1+p_{z1}}{E_1-p_{z1}}\frac{E_2-p_{z2}}{E_2+p_{z2}}} + \sqrt{\frac{E_1-p_{z1}}{E_1+p_{z1}}\frac{E_2+p_{z2}}{E_2-p_{z2}}} \tag{A.3}$$

$$= \frac{(E_1+p_{z1})(E_2-p_{z2})}{\sqrt{E_1^2-p_{z1}^2}\sqrt{E_2^2-p_{z2}^2}} + \frac{(E_1-p_{z1})(E_2+p_{z2})}{\sqrt{E_1^2-p_{z1}^2}\sqrt{E_2^2-p_{z2}^2}} \tag{A.4}$$

Using $E - p_z = \sqrt{m^2+p_T^2} = E_T$:

$$= \frac{(E_1+p_{z1})(E_2-p_{z2})+(E_1-p_{z1})(E_2+p_{z2})}{\sqrt{m_1^2+p_{T1}^2}\sqrt{m_2^2+p_{T2}^2}} = 2\frac{E_1E_2-p_{z1}\cdot p_{z2}}{E_{T1}E_{T2}} \tag{A.5}$$

Plugging this expression for $2\cosh\Delta\eta$ yields a useful kinematic result:

$$m_{12}^2 = m_1^2+m_2^2+2(E_1E_2-p_1\cdot p_2) = m_1^2+m_2^2+2(E_{T1}E_{T2}\frac{E_1E_2-p_1\cdot p_2}{E_{T1}E_{T2}}) \tag{A.6}$$

$$m_{12}^2 = m_1^2 + m_2^2 + 2(E_{T1}E_{T2}\cosh\Delta\eta - p_{T1}\cdot p_{T2}) \tag{A.7}$$

In the context of our 2-jet VBF signature ($m^{jet} << p_T^{jet}$), and considering that $E_T \cong |p_T|$

$$m_{jj} \cong \sqrt{2(|p_T^{jet1}||p_T^{jet2}|\cosh\Delta\eta} \tag{A.8}$$

Whether $\Delta\eta$ is positive or negative, $\cosh\Delta\eta \sim e^{|\Delta\eta|}$. Also, assuming that the transverse momentum kick for our two jets is similar ($|p_T^{jet1}| \sim |p_T^{jet2}|$), we have:

$$m_{jj} \cong e^{\frac{|\Delta\eta|}{2}}\sqrt{2(|p_T^{jet1}||p_T^{jet2}|} \tag{A.9}$$

Thus m_{jj}, $\Delta\eta$ and p_T^{jet} are directly correlated. $\square$

APPENDIX B

SUSY MIXING MATRICES

Though the SUSY Lagrangian density is often formulated in terms of $\tilde{B}$, $\tilde{W}$, and $\tilde{H}$, our observable particles are neutralinos ($\tilde{\chi}^0$) which are some linear combination of the aforementioned partilces. This is because the mass term of our Lagrangian contains cross-terms between fields, allowing mixing. For example, here is the MSSM soft SUSY breaking Lagrangian in MSSM (See p. 56 [20].)

$$\begin{aligned} \mathcal{L}_{Soft}^{MSSM} &= -\frac{1}{2}(M_3\tilde{g}\tilde{g} + M_2\tilde{W}\tilde{W} + M_1\tilde{B}\tilde{B} + c.c.) \\ &+ ... - m_{H_u}^2 H_u^* H_u - m_{H_d}^2 H_d^* H_d - (bH_u H_d + c.c.) \end{aligned} \tag{B.1}$$

With certain simplifying assumptions, we can arrive at the mSUGRA neutralino mass matrix:

$$\begin{bmatrix} \widetilde{\chi}_i^0 \\ \widetilde{\chi}_j^0 \\ \widetilde{\chi}_k^0 \\ \widetilde{\chi}_l^0 \end{bmatrix} = \begin{bmatrix} M_1 & 0 & -m_Z s_W \cos\beta & m_Z s_W \sin\beta \\ 0 & M_2 & m_Z c_W \cos\beta & -m_Z c_W \sin\beta \\ -m_Z s_W \cos\beta & m_Z c_W \cos\beta & 0 & -\mu \\ m_Z s_W \sin\beta & -m_Z c_W \sin\beta & -\mu & 0 \end{bmatrix} \begin{bmatrix} B \\ W \\ H_1^0 \\ H_2^0 \end{bmatrix}$$

Were no cross-terms to arrive, we would have a perfectly diagonal matrix (as can be witnessed by the $M_1\tilde{B}\tilde{B}$, $M_2\tilde{W}\tilde{W}$ terms). Cross-terms do arise however, and mixing occurs between the neutralino mass eigenstates. It is for this reason that the composition of our neutralinos varies in $\tilde{B}$, $\tilde{W}$, and $\tilde{H}$ as we move through SUSY

parameter space.

APPENDIX C

THE BINOMIAL DISTRIBUTION IN LARGE N AND POISSON STATISTICS

The binomial distribution is given by:

$$B_{n,p}(\nu) = \frac{n!}{\nu!(n-\nu)!}p^{\nu}(1-p)^{n-\nu} \tag{C.1}$$

where p is the probability for a single trial and $B_{n,p}(\nu)$ is the probability of ν occurrences in n trials. For large n, we have:

$$B_{n,p}(\nu) \approx \frac{n(n-1)...(n-\nu)}{\nu!}p^{\nu}(1-p)^{n} \approx \frac{(np)^{\nu}}{\nu!}(1-p)^{n} = \frac{\mu^{\nu}}{\nu!}(1-p)^{n} \tag{C.2}$$

where $\mu = np$ is the average number of occurrences. Defining $x = (1-p)^n$ we see:

$$\frac{dx}{dp} = -n(1-p)^{n-1}; \frac{d^2x}{dp^2} = n(n-1)(1-p)^{n-2}; \frac{d^mx}{dp^m} = n(n-1)...(n-m)(1-p)^{n-m} \tag{C.3}$$

From which Brook Taylor and his famous theorem tells gives us:

$$x = (1-p)^n = 1 - np + \frac{n(n-1)p^2}{2} - ... + (-1)^m\frac{n(n-1)...(n-m)p^m}{m!} \tag{C.4}$$

$$x = (1-p)^n \approx 1 - \mu + \frac{\mu^2}{2} - ... + (-1)^m\frac{\mu^n}{m!} = e^{-\mu} \tag{C.5}$$

And now we have arrived at the Poisson distribution:

$$B_{n,p}(\nu) \approx e^{-\mu}\frac{\mu^{\nu}}{\nu!} = P_{\mu}(\nu) \tag{C.6}$$

Note that by assuming large n, we have gotten rid of this variable entirely. In the case we are thinking of luminosity, it is much more convenient to think of the probability of ν collisions as given by Poisson statistics rather than binomial statistics for many reasons. One of the more subtle reasons is that we no longer need to factor in how many possible collisions there were (how many combinations of protons could interact). We simply need to know the instantaneous luminosity or the mean number of interactions and we know the probability of any number of simultaneous collisions (the 'pileup' distribution). It is certainly fair to approximate n to be large when considering luminosity as each proton bunch in the LHC has $\mathcal{O}(10^{11})$ protons, so there are $\mathcal{O}(10^{22})$ possible collisions.